

Time-Resolved Photoresponse Studies of
Ferromagnet/Superconductor Nano-
Bilayers and Nanostructures

by

Dong Pan

Submitted in Partial Fulfillment
of the
Requirements for the Degree
Doctor of Philosophy

Supervised by

Professor Roman Sobolewski

Department of Physics and Astronomy
Arts, Sciences and Engineering
School of Arts and Sciences

University of Rochester
Rochester, New York

2010

To my wife,
Annie Xiaohong Zhang

Curriculum Vitae

Dong Pan was born in Tianjin, China on June 12th, 1977. He attended Nankai University from 1994 to 2001, and graduated with Double-Bachelors of Science and Law degrees in 1998 and the Master of Optical Engineer degree in 2001. He came to the University of Rochester in the fall of 2002 and began graduate studies in the Department of Physics and Astronomy. He received the Master of Arts degree from the Department of Physics and Astronomy, University of Rochester in 2004 and received the Master of Science degree from The Institute of Optics in 2005. He was granted the Frank Horton Graduate Fellowship from the Laboratory for Laser Energetics from 2003 to 2005. He continued the pursuit of the Doctor of Philosophy degree under the guidance of Professor Roman Sobolewski. His research interests include ultrafast carrier dynamics under optical excitation and fast photodectors of low temperature and high temperature superconductor material. He is a member of the IEEE and the American Physical Society.

Acknowledgements

I have been very fortunate to have the privilege of working with Professor Roman Sobolewski, which turned out to be an exciting and rewarding learning experience. It is his sharp insight, enlightened guidance, and generous support that made it possible for me to finish a project like this. He also took a genuine interest in my personal development and ensured my growth by constant demands, advice and encouragement. I deeply appreciate the best of opportunities Professor Sobolewski provided me, and credit his belief in my capabilities as an inspiration for achievement of my academic career.

I would like to thank all the members (both past and present) in the ultrafast optoelectronics research community at the Laboratory for Laser Energetics. Along with other members of the Department of Physics and Astronomy, they have made my graduate study fruitful. I would appreciate the friendship and help in various manners from Shuai Wu, Marat Khafizov, Daozhi Wang, Allen Cross, Xia Li Cross, Jennifer Kitaygorsky, Cheng Zhao, Jie Zhang, Hiroshi Irie, Gregg Guarino, and Takahiro Taneda. I am particularly thankful to Dr. Ivan Komissarov for his team work with me to overcome many problems and frustrations I experienced in my experiments early years.

My graduate experience has been enhanced through the collaboration with the CNR-INFN Coherentia and Dipartimento Scienze Fisiche, Università di Napoli "Federico II", ITALY. I am grateful to Professor Giovanni Piero Pepe for research discussion and providing me very high-quality samples.

I would also like to express my gratitude to my family for their support and patience throughout many years of my school study. Finally, but most heartily, I would thank my wife, Annie Xiaohong Zhang, for her deep love, understanding, support, and tolerance.

The work of my thesis research was partially supported by the MIUR COFIN 2007–2009 “Effetti Quantistici in Nano-strutture e Dispositivi Superconduttivi” (Napoli), by the USAFOSR under Grant No. FA9550-06-1-0348, and the NYSTAR grant to the University of Rochester CAT-EIS (Rochester). During the latest phase of research partial support came from the NSF ECCS grant No. 0824075.

Abstract

Interactions of superconducting nanostructures with external ultrafast optical radiation represent a very interesting topic in both the framework of nonequilibrium physics and photodetector applications. Heterogeneous proximized ferromagnet/superconductor nano-bilayers are very promising since they exhibit the ultrafast Cooper-pair and quasiparticle dynamics.

In this thesis, to study on the role of proximity effect on electron-phonon coupling in F/S heterostructures, we have characterized NiCu/Nb, NiCu/Au/YBaCuO, and LaSrMnO/YBaCuO nano-bilayers, using time-resolved, all optical, femtosecond pump-probe spectroscopy method and transient photoimpedance measurement. We fitted the experimental data with the two-temperature (2-T) model and our own extension model, the three-temperature (3-T) model, which involves relaxation quasiparticles with both optical and acoustic phonons. The 3-T model gives more accurate fitting results than the 2-T model. Moreover, our time-resolved studies of the carrier dynamics in oxide-based F/S structures open the way to novel basic-physics investigations of nonequilibrium effects in correlated systems. Our research results demonstrate that the F/S nanobilayers represent a new class of designed superconducting structures, which can be used in future for ultrafast photodetectors.

Table of Contents

Dedication	ii
Curriculum Vitae	iii
Acknowledgements	iv
Abstract.....	vi
Table of Contents	vii
List of Tables	x
List of Figures	xi
List of Symbols	xiv
Foreword.....	1
Chapter 1. Introduction.....	2
1.1 Motivation of the thesis	2
1.2 General properties of normal-metal/superconductor nano-bilayers	4
1.3 The superconducting state: nonequilibrium vs. bolometric effects	7
1.4 Outline of the thesis	9
References.....	11
Chapter 2. Nonequilibrium carrier dynamics in superconductors.....	15
2.1 Optical photoexcitation of superconductors	15
2.2 Thermodynamics of the superconducting state.....	20

2.3	Rothwarf-Taylor model	23
2.4	Two-temperature model.....	26
2.5	Three-temperature model.....	31
2.6	Kinetic-inductive effects.....	34
	References.....	39
Chapter 3. Ferromagnet/Superconductor nano-bilayers: sample characterization, and transient photoresponse experimentation		43
3.1	Nano-bilayers fabrication and patterning.....	43
3.2	Structural and electrical characterization of bilayers.....	46
3.3	Femtosecond, all-optical time-resolved spectroscopy	50
	3.3.1 Principle of pump-probe transient reflectivity experiments	51
	3.3.2 Experimental setup.....	53
3.4	Time-resolved photoimpedance studies	55
	References.....	58
Chapter 4. Time-resolved dynamics of carriers in NiCu/Nb nano-bilayers.....		60
4.1	Transient reflectivity experiment results	60
	4.1.1 Two-temperature model fitting of NiCu/Nb and Nb samples	63
	4.1.2 The concept of the three-temperature model and fitting results.....	67
4.2	Transient photoimpedance experiment results.....	72
	4.2.1 Kinetic-inductive photoresponse transients of NiCu/Nb microbridges ..	73
	4.2.2 Bolometric photoresponse transients of Nb microbridges.....	75
4.3	Summary	77
	References.....	78
Chapter 5. Transient reflectivity measurements of F/S hetero-structures formed by perovskite oxide materials		79
5.1	NiCu/YBCO F/S nano-bilayers	83

5.2	LSMO/YBCO F/S nano-bilayers	86
5.3	Summary.....	90
	References	91
Chapter 6. Conclusions.....		93
6.1	Thesis summary and the main results.....	93
6.2	Directions for future work	95

List of Tables

Table 3.1	Summarization of the concentration of Ni and Cu at the five points, setting the sum of those concentration to be 100 atomic % [2]	48
Table 3.2	Ni _{0.48} Cu _{0.52} /Nb and pure Nb sample specifications	56
Table 4.1	Summarization of the τ_{e-Oph} and τ_{e-Aph} values in the 3-T model fitting results and τ_{fast} and τ_{slow} components in Taneda <i>et al.</i> 's [1] two-exponential numerical method.....	71

List of Figures

Figure 1.1 The decay of order parameter in the normal (N) layer and in the ferromagnet (F) layer. (a) The order parameter in the N layer shows monotonic decay. (b) The order parameter in the F layer shows damped oscillatory behavior.....	4
Figure 2.1 Simplified energy band diagrams of semiconductors (a) and superconductors (b). Energies $\hbar\omega \geq E_g$ can create electron-hole pairs in a semiconductor, or break Cooper pairs in a superconductor to create highly excited electrons if $\hbar\omega \geq 2\Delta$	17
Figure 2.2 Schematics of carrier dynamics in the superconducting state under optical excitation.....	24
Figure 2.3 Energy flow and its relaxation time among the electron and phonon subsystems and the substrate in the 2-T model.....	28
Figure 2.4 Energy flow among the electron subsystem, optical phonon subsystem and acoustical phonon subsystem in the 3-T model.....	32
Figure 2.5 Measured photoresponse of a YBCO microbridge at $T = 80$ K when the bridge was biased in the resistive hot-spot state, and fitted with the nonequilibrium electron heating two-temperature photoresponse model [20].....	35
Figure 2.6 Measured kinetic inductive voltage photoresponse of a YBCO microbridge (solid dots) fitted using R-T model (solid line) at temperature below T_c [25].....	38
Figure 3.1 Schematics of the F/S nano-bilayer.....	44
Figure 3.2 TEM image of the cross section of NiCu (6 nm)/Nb (60 nm) bilayer film [2].....	47
Figure 3.3 Critical current density dependence on temperature for NiCu/Nb and Nb microbridges. The inset shows the actual I - V characteristics in the semilogarithmic scale of both samples taken at 8 K.....	49
Figure 3.4 Principle of the pump-probe experiments	52

Figure 3.5 Pump-probe experimental setup for transient reflectivity measurement	54
Figure 3.6 Time-resolved photoimpedance experiment setup.....	57
Figure 4.1 Normalized reflectivity change $\Delta R/R$ as a function of the time delay [1]	61
Figure 4.2 Normalized reflectivity change as a function of time (open circles), measured at 6 K for (a) NiCu/Nb and (b) Nb samples. The solid lines are the electron and phonon temperature transients, respectively, numerically evaluated for our films using the 2-T model [see Eq. (2.19) and Eq. (2.20)]. The right y axes show the actual increase in the electron/phonon temperature [3]	64
Figure 4.3 Time-resolved $\Delta R/R$ waveforms (semi-log scale) observed in a Nb(70 nm) thin film (red squares) and a NiCu (21 nm)/Nb (70 nm) bilayer (blue triangles) measured at T = 6 K	68
Figure 4.4 Numerical evaluation of the electron, optical phonon, acoustical phonon temperature transients for (a) pure Nb (70 nm), (b) NiCu (6 nm)/Nb (70 nm), (c) the same data as in (b) but in the semi-log scale, (d) NiCu (21 nm)/Nb (70 nm) and (e) the same data as in (d) but in the semi-log scale using the 3-T model [see Eq. (2.26) to Eq. (2.28)].....	71
Figure 4.5 Numerical simulations of V_{kin} as a function of time, obtained using the 2-Tmodel solutions plotted in Fig. 4.2 and Equations (2.31) and (2.32), for our NiCu/Nb (large oscillatory curve) and Nb (inset) samples. The bias current in both cases was $I_b/I_c = 0.43$	72
Figure 4.6 Experimental photoresponse transient of a NiCu/Nb microbridge, acquired at 6 K with $I_b = 4.5$ mA ($I_b/I_c = 0.43$). The solid (red) line is the fit based on the kinetic-inductive model [see Fig. 4.5], numerically stretched in order to account for the limited bandwidth of our output amplifier	74
Figure 4.7 Experimental photoresponse transient of a pure Nb microbridge, acquired at 7 K with $I_b/I_c = 0.43$. The solid (red) line is the fit	

based on the simple-resistive model [see Eq. (2.30)]. The incident optical pulse repetition time was 20 ns	76
Figure 5.1 The unit cell of $\text{YBa}_2\text{Cu}_3\text{O}_{7-\delta}$ showing the location of the CuO_2 planes which are believed to contain the superconducting current.....	81
Figure 5.2 Time-resolved $\Delta R/R$ waveforms (semi-log scale) observed in a 100-nm YBCO thin film (black squares) and a NiCu (12 nm)/Au (10 nm)/YBCO (100 nm) bilayer (red open circles) measured at $T = 5$ K. The dashed lines are bi-exponential fits	84
Figure 5.3 Numerical evaluation of the electron, optical phonon, acoustical phonon temperature transients for NiCu (12 nm)/Au (10 nm)/YBCO (100 nm) bilayer using the 3-T model [see Eq. (2.26) to Eq. (2.28)]	85
Figure 5.4 Direct-current (dc) conductivity versus temperature of a LSMO film.....	86
Figure 5.5 Time-resolved $\Delta R/R$ waveforms (semi-log scale) observed in a 100-nm YBCO thin film (black squares) and a LSMO (10 nm)/YBCO (100 nm) (red open circles) measured at $T = 20$ K	87
Figure 5.6 Numerical evaluation of the electron, optical phonon, acoustical phonon temperature transients for LSMO (10 nm)/YBCO (100 nm) bilayer using the 3-T model [see Eq. (2.26) to Eq. (2.28)]	88

List of Symbols

AFM	Atomic Force Microscope
A_{ph}	acoustic phonon
BCS	Bardeen, Cooper, Schrieffer superconductivity theory
β	pair-braking rate
β_3	phonon specific heat constant
γ	Sommerfield constant
C	specific heat
C_e	electron specific heat
C_p	phonon specific heat
C_{Aph}	acoustic phonon specific heat
C_{Oph}	optical phonon specific heat
CSL	coplanar stripline
d	thickness of the film/microbridge
DoS	density of state
Δ (T)	superconducting energy gap
$\Delta R/R$	transient reflectivity signal
E	energy
E_g	energy gap
e	electron charge
EDX	Energy-Dispersive X-ray spectroscopy
ε	quasiparticle kinetic energy

F	ferromagnet
$F(\omega)$	the Debye phonon density of states
FM	ferromagnetic
f_{sc}	superfluid fraction
g_{e-ph}	electron phonon coupling constant
Ψ	superconductor-order parameter
\hbar	Plank's constant
HTS	high-temperature superconductor
I_b	bias current
I_c	critical current
I(t)	laser source for optical excitation
J_c	critical current density
k_B	Boltzmann's constant
l	length of the microbridge
L_{kin}	kinetic inductance
LSMO	LaSrMnO
LTS	low-temperature superconductor
λ_L	magnetic penetration depth
n_q	quasiparticle concentration
n_{qT}	thermal equilibrium quasiparticle concentration
N	normal metal
N_ω	2Δ -phonon concentration
$N_{\omega T}$	thermal equilibrium 2Δ -phonon concentration

$N(0)$	electron density of states at the Fermi level.
v	ion density
Oph	optical phonon
PLD	pulsed laser deposition
ph	phonon
PM	paramagnetic
QP	quasiparticle
R	resistance
R	QP recombination rate
R_B	thermal boundary resistance between thin film and substrate
RT	Rothwarf-Taylor model
S	superconductor
σ_n	normal state conductivity
t	time
T	temperature
T_c	superconducting transition temperature
T_{Cu}	Curie temperature
T_{ph}	phonon subsystem temperature
T_b	substrate temperature
T_e	electron temperature
TEM	Transmission Electron Microscope
T_{ph}	phonon temperature
T_{Aph}	acoustic phonon temperature

T_{Oph}	optical phonon temperature
τ_T	electron scattering time
τ_{es}	phonon escape time
τ_{fast}	fast decay time constant
τ_{slow}	slow decay time constant
τ_{e-ph}	electron- phonon scattering time
τ_{e-Aph}	electron- acoustic phonon scattering time
τ_{e-Oph}	electron-optical phonon scattering time
τ_{ph-e}	phonon-electron scattering time
τ_{Aph-e}	acoustic phonon-electron scattering time
τ_{Oph-e}	optical phonon-electron scattering time
V_C	combined kinetic-inductive and resistive voltage response
V_{ep}	electron-phonon coupling strength
V_{kin}	kinetic-inductive voltage response
V_r	resistive voltage response
w	width of the microbridge
ω	frequency
ω_p	plasma frequency of the superconductor
ω_D	Debye phonon frequency
ξ	coherence length
YBCO	$YBa_2Cu_3O_{7-\delta}$
2-T	two temperature model
3-T	three temperature model

Foreword

The author performed all experimental procedures, data analysis, and fitting in this thesis unless specified below. Sample fabrication was done at the University of Naples, Italy, as part of our collaborative research.

Chapter 3, Figure 3.2: “The TEM image of the cross section of NiCu (6 nm)/Nb (60nm) bilayer film” was provided by courtesy of our collaborators in the University of Naples in Italy, Professor Giovanni Piero Pepe’s group.

Chapter 4, the time-resolved $\Delta R/R$ waveforms used in this work to perform data analysis of Nb and NiCu/Nb films were measured by Takahiro Taneda in the lab of Professor Roman Sobolewski, University of Rochester.

Chapter 5, the time-resolved $\Delta R/R$ waveforms of an YBCO thin film, and NiCu/Au/YBCO and LSMO/YBCO bilayers were measured by Nicola Marrocco and Loredana Parlato in the lab of Professor Giovanni Piero Pepe, University of Naples in Italy. Data analysis was done jointly by the UR and U of N groups.

Chapter One: Introduction

1.1 Motivation of the thesis

Superconducting devices based on both low- and high-temperature superconductors (LTSs and HTSs) have been proposed for many radiation detection applications ranging from deep-space radio astronomy to fiber-based single-photon telecommunications due to their sensitivity over a very wide frequency range (from X-ray, through optical wavelengths to THz radiation) [1,2], ultra-fast electronic response times (down to few picoseconds) [3], and radiation hardness qualification [4]. The superconductor response to the radiation interaction after the absorption of radiation quanta involves complex dynamics, which depends on the relaxation processes involving phonons, quasiparticles (QPs), and Cooper pairs during the energy cascade [2]. The mean energy required to break a Cooper pair for creating an excitation is at least equal to the superconductor energy gap 2Δ (order of few meV), and hence three orders of magnitude smaller than the energy gap in a typical semiconductor [5]. The small value of Δ enables generation of an efficient avalanche of excited QPs in a superconducting material, even upon absorption of an infrared optical photon [6]. The QP multiplication effect enhances resolution in energy-resolving superconducting devices, such as superconducting tunnel junctions (STJ) [7]. Simultaneously, the energy-relaxation time constants of QPs in thin- and

ultrathin-film structures of LTSs and HTSs, respectively, are in the picoseconds range which makes GHz detection rates possible with proper superconductive structure configurations [8,9]

The proximity effect in ferromagnet-superconductor (F/S) heterostructures represents a new and intriguing research area in superconducting devices both from the basic physics and application points of view [10,11]. Superconductivity and ferromagnetism have competing long-term orders. The Cooper pairs in a conventional S form singlet pairing, while spins in the F prefer the parallel alignment. When an F layer is in contact with an S layer, superconductivity is suppressed by ferromagnetism due to exchange interaction, which prefers parallel spin orientation.

In order to understand the proximity effect in detail between the S and F, various forms of F/S hybrid structures have been extensively studied [12]. Though the coexistence of singlet superconductivity with ferromagnetism is very unlikely in bulk compounds, it can be easily achieved in artificially fabricated layered F/S systems. Unlike the simple exponential decay of the superconductor-order parameter (Ψ) in the conventional proximity effect that occurs at the interface between normal metal and superconductor (N/S structures) as shown in Fig. 1.1(a), the proximity effect in the F/S system shows damped oscillatory behavior of the Cooper pair wave function within the ferromagnetic medium, as shown in Fig. 1.1(b) [11,13]. As a result, the critical temperature of the F/S bilayer (or multilayer) depends non-monotonically on the ferromagnetic layer thickness [14].

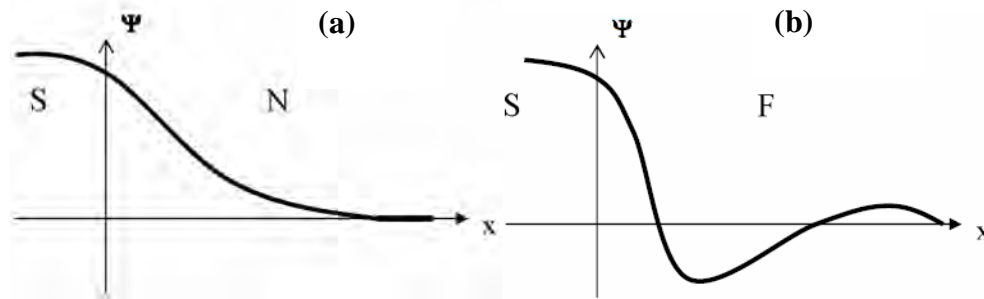


Figure 1.1: The decay of order parameter in the normal (N) layer and in the ferromagnet (F) layer. (a) The order parameter in the N layer shows monotonic decay. (b) The order parameter in the F layer shows damped oscillatory behavior.

Very few studies have been done so far on the time-resolved dynamics of Cooper pairs and QPs in the F/S system. The purpose of my thesis research is to investigate nonequilibrium carrier dynamics in nanostructured F/S bilayers. The emphasis of my research is on the ultrafast QP relaxation process in the F/S system by using femtosecond, optical pump-probe spectroscopy system to measure the transient reflectivity change and performing transient photoimpedance measurements on microbridges and nanobridges made of different F/S bilayers, composed of various superconductor and ferromagnetic materials.

1.2 General properties of normal-metal/superconductor nano-bilayers

The contact of materials with different long-range ordering modifies their properties near the interface. In the case of a N/S interface, the Cooper pairs can penetrate the normal metal at some distance. Therefore, superconducting like properties may be

induced in the normal metal, and this phenomenon is called the proximity effect [15]. Simultaneously, leakage of the Cooper pairs weakens the superconductivity near the interface with a normal metal. This effect is called the inverse proximity effect, and results in a decrease of the superconducting transition temperature (T_c) in a thin superconducting layer in contact with a normal metal. If the superconducting layer is thinner than a certain critical thickness, the proximity effect may totally suppress the superconducting transition [11].

Heterogeneous structures formed by a S and a N layers in contact represent a novel and promising research area [16]. According to the physics principle of the proximity effect, near the N/S plane, both materials influence each other on a spatial scale of their coherence lengths, ξ_N and ξ_S , respectively. Since Cooper pairs can penetrate into the normal metal with a finite lifetime, superconducting correlations are induced in the normal metal. The physical properties of the bilayer are generally determined by the N material deposited on top of the S film. If the N layer is thinner than a certain critical thickness, it acts just like a thermometer for the electron temperature T_e of the underlying S layer, while it is transparent to phonons [17]. For thicker N overlayers, the carrier and phonon distributions are coupled through suitable boundary conditions at the interface and the interaction is reflected on a spatial variation of the density of states (DoS), directly affecting the electron and phonon lifetimes. In well-investigated proximized bilayers, such as Al/Nb, Ta/Nb, or Al/Ta, the N/S interface is highly transparent and ξ_N and ξ_S are usually much larger than the material's optical penetration depth α , which in metals is typically below 50

nm at 400–900 nm wavelength range. The laser probe beam in pump-probe experiments can only sense the carrier dynamics of the top layer (N layer), far away from the interface between N and S layers. On the other hand, an optically thin N layer represents a too small perturbation in order to optically measure any proximity-related effects.

The solution, presented in this thesis, is the implementation of a ferromagnet as the top layer, forming F/S bilayers. In such hybrid structures, Ψ decays over a distance of the order of a few nanometers since $\xi_F \leq 10$ nm and can be modulated by a proper choice of the magnetic exchange energy by varying the thickness of the F film[18]. The F/S proximity bilayers are unique in this context due to the presence of the magnetic exchange energy. Especially in weak F/S heterostructures, the superconducting properties vary significantly over the distance comparable to the penetration depth α of the visible light into our metallic material. In general, the coexistence of the F and S states is a very promising in the quest for the ultrafast QP dynamics. The related research topics have great potential in applications, ranging from quantum electronics (spintronics) devices [19] to novel ultrafast photodetection [20]. Moreover, the ultrafast dynamics in F/S structures based on oxide superconductors opens the way to interesting basic physics investigations.

1.3 The superconducting state: nonequilibrium vs. bolometric effects

The mechanisms responsible for detection of optical radiation by superconductors can be divided into two classes: equilibrium (bolometric) and nonequilibrium (non-bolometric) modes [21]. Both bolometric and non-bolometric mechanisms are present in most superconducting devices. In the equilibrium mode, the superconductor responds to a change in lattice temperature which is mostly determined by low-energy acoustic phonons, and acts like a sensitive thermometer. In such case, both the electron and the phonon subsystems remain in thermal equilibrium and experience the same temperature shift after the optical excitation process. The relaxation time is not governed by the electrons but the phonons, which exhibit slower relaxation on the order of nanoseconds or even microseconds. Bolometric response is a sensitive radiation detection mechanism and has been very well understood [22].

The nonequilibrium response is produced by photons breaking Cooper pairs, creating high-energy QPs and, subsequently, high-energy phonons [23]. The electron subsystem and the phonon subsystem are decoupled and each follows a different time evolution during their relaxation. Initially, only electron states are changed by the radiation, while the phonon subsystem remains in the thermodynamics equilibrium with the substrate and plays the role of a heat sink for electrons. In both equilibrium and nonequilibrium effects, the correction to the QP distribution function due to optical excitation gives rise to a change of macroscopic properties such as resistivity, kinetic inductance, or magnetic flux. The nonequilibrium detection mechanism based

on the kinetic inductance change is intrinsically much faster and less demanding in terms of the biasing condition than a more standard resistive (bolometric) photoresponse, based on the nonlinear, resistivity vs. temperature dependence near T_c .

The ability to generate electrical signals due to photoexaction is the basis for any photodetectors. From the application point of view, the nonequilibrium processes in superconductors can lead to the photonresponse with subpicosecond time characteristics. It opens possibilities for the design of extremely energy-sensitive and ultrafast devices for radiation detection [18,24].

1.4 Outline of the thesis

This thesis is focused on investigating basic carrier dynamics in nanostructured F/S bilayers, with the main emphasis on the ultrafast QP relaxation process in the F/S system, studied by the femtosecond, optical pump-probe technique and transient photoimpedance method. The remainder of the thesis is arranged in five chapters.

In Chap. 2, the physics of the carrier dynamics in a photoexcited superconducting material is described. First, a qualitative picture of QP generation via photoexcitation, their recombination into Cooper pairs, and comparison with photoexcited semiconductor are shown. After that I will present some basic theory of thermodynamics in the superconducting state and current theoretical models that are used to describe the nonequilibrium carrier dynamics of the superconducting state. These models include the Rothwarf-Taylor (RT) model and two-temperature (2-T) model. In addition, I will introduce our own, three-temperature (3-T) model, which involves relaxation QPs with both optical and acoustic phonons. The solutions of the above models will provide the theoretical descriptions for our data analysis for both the all optical photoresponse (pump-probe) and the kinetic-inductive response.

In Chap. 3, I introduce fabrication processes of F/S nano-bilayer samples and electrical characterization of bilayers. Then the femtosecond, all-optical time-resolved spectroscopy will be presented, which includes the principle of pump-probe transient reflectivity experiments and its experimental setup. The transient photoimpedance

experiments used to study another macroscopic physical property of the F/S bilayer will also be described in this chapter.

Chapter 4 is devoted to explain our experimental results of both the transient reflectivity change induced under femtosecond optical excitation and the transient photoimpedance signal generated by an optically-excited, current-biased superconducting microbridge. Model fitting of experimental results of NiCu/Nb and pure Nb samples will be shown. I will fit our experimental data using our 3-T model and compare the results with the 2-T model fittings. Finally, the R-T and bolometric models will be used to analyze our photoimpedance studies.

In Chap. 5, transient reflectivity measurements results and analysis of novel F/S heterostructures formed by perovskite oxide materials, NiCu/Au/YBaCuO(YBCO) F/S nano-bilayers and LaSrMnO(LSMO)/YBCO F/S nano-bilayers, will be shown.

Finally, Chap. 6 summarizes the accomplishments of the work performed in this thesis and presents some ideas for future investigations.

References:

- ¹ P. K. Day, H. G. LeDuc, B. A. Mazin, A. Vayonakis, and J. Zmuidzinas. A broadband superconducting detector suitable for use in large arrays. *Nature*, 425:817–821 (2003).
- ² A. Semenov, G. N. Gol'tsman, and R. Sobolewski. Hot-electron effect in superconductors and its applications for radiation sensors. *Supercond. Sci. and Technol*, 15, R1–R16 (2002).
- ³ M. Lindgren, M. Currie, C. Williams, T.Y. Hsiang, P.M. Fauchet, R. Sobolewski, S.H. Moffat, R.A. Hughes, J.S. Preston, and F.A. Hegmann. Intrinsic Photoresponse Times of Y-Ba-Cu-O Superconducting Photodetectors. *Appl. Phys. Lett.*, 74, 853 (1999).
- ⁴ A. Peacock, P. Verhoeve, N. Rando, A. van Dordrecht, B. G. Taylor, C. Erd, M. A. C. Perryman, R. Venn†, J. Howlett, D. J. Goldie, J. Lumley and M. Wallis. Single optical photon detection with a superconducting tunnel junction, *Nature*, 381, 135 (1996).
- ⁵ A. Barone, M. Ejrnes, E. Esposito, R. Latempa, S. Pagano, L. Parlato, and G. P. Pepe. Superconductive radiation detectors: challenges and some recent achievements. *Physica Status Solidi*, 3, 9, 3104 – 3109 (2006).
- ⁶ G. N. Gol'tsman, O. Okunev, G. Chulkova, A. Lipatov, A. Semenov, K. Smirnov, B. Voronov, A. Dzardanov, C. Williams, and R. Sobolewski. Picosecond superconducting single-photon optical detector. *Appl. Phys. Lett.*, 79, 705 (2001).

-
- ⁷ J. N. Ullom, P. A. Fisher, and M. Nahum, *Appl. Phys. Lett.* **73**, 2494 (1998).
- ⁸ G. Gol'tsman, O. Minaeva, A. Korneev, M. Tarkhov, I. Rubtsova, A. Divochiy, I. Milostnaya, G. Chulkova, N. Kaurova, B. Voronov, D. Pan, J. Kitaygorsky, A. Cross, A. Pearlman, I. Komissarov, W. Słysz, M. Węgrzecki, P. Grabiec, and R. Sobolewski. Middle-Infrared to Visible-Light Ultrafast Superconducting Single-Photon Detectors. *IEEE Trans. Appl. Supercon.*, **17**, 2, 246 (2007).
- ⁹ A. Barone and G. Paternó, *Physica Status Solidi C: Current Topics in Solid State Physics* **3** (9) 3104 (2006).
- ¹⁰ A. A. Golubov, E. P. Houwman, J. G. Gijsbertsen, J. Flokstra, H. Rogalla, J. B. le Grand, and P. A. Korte. Quasiparticle lifetimes and tunneling times in a superconductor-insulator-superconductor tunnel junction with spatially inhomogeneous electrodes. *Phys. Rev. B*, **49**, 12953 (1994).
- ¹¹ A. I. Buzdin. Proximity effects in superconductor-ferromagnet heterostructures. *Reviews of Modern Physics*, **77**, 935 (2005).
- ¹² Dong Ho Kim and T. J. Hwang. Superconductivity in narrow-band systems with local nonretarded attractive interactions. *Physica C*, **455**, 58–62 (2007).
- ¹³ E. A. Demler, G. B. Arnold, and M. R. Beasley. Superconducting proximity effects in magnetic metals. *Phys. Rev. B* **55**, 15174-15182 (1997).
- ¹⁴ A. I. Buzdin, and M. Y. Kuprianov, *Pis'ma Zh. Eksp. Teor. Phys.*, **52**, 1089-1091 (1990) [*JETP Lett.* **52**, 487-491 (1990)].

-
- ¹⁵ A. Barone and G. Paternó, *Physics and Applications of the Josephson Effect*, Wiley, New York. (1982).
- ¹⁶ E. Esposito, G. Pepe, and U. Scotti di Uccio. The relaxation times of an STJ detector: Role of the proximity effect. *J. Supercond.*, 7, 951 (1994).
- ¹⁷ S. D. Brorson, A. Kazeroonian, J. S. Moodera, D. W. Face, T. K. Cheng, E. P. Ippen, M. S. Dresselhaus, and G. Dresselhaus. Femtosecond room-temperature measurement of the electron-phonon coupling constant γ in metallic superconductors. *Phys. Rev. Lett.*, 64, 2172 (1990).
- ¹⁸ T. Taneda, G.P. Pepe, L.Parlato, A.A. Golubov, and R. Sobolewski. Time-resolved carrier dynamics and electron-phonon coupling strength in proximized weak ferromagnet-superconductor nanobilayers. *Phys. Rev. B*, 15, 174507 (2007).
- ¹⁹ G. Blatter, V. B. Geshkenbein, and L. B. Ioffe. Design aspects of superconducting-phase quantum bits. *Phys. Rev. B*, 63, 174511 (2001).
- ²⁰ A. A. Golubov, M. Yu. Kupriyanov, and E. Il'ichev, *ibid.* 76, 411 (2004); F. S. Bergeret, A. F. Volkov, and K. B. Efetov, *ibid.* 77, 1321 (2005).
- ²¹ A. Frenkel, Frenkel-Kontorova model with a transversal degree of freedom: Static properties of kinks. *Phys. Rev. B*, 48, 13, 3737. (1993)
- ²² J. Clarke, G. I. Hoffer, P. L. Richards, and N. H. Yeh. Superconductive bolometers for submillimeter wavelengths. *J. Appl. Phys.*, 48, 4865 (1977)

²³ N. Bluzer, Temporal relaxation of nonequilibrium in Y-Ba-Cu-O measured from transient photoimpedance response. *Phys. Rev. Lett.*, 44, 10222 (1991).

²⁴ D. N. Langenberg and A. I. Larkin, Nonequilibrium Superconductivity, *Modern Problems in Condensed Matter Sciences*, 12. (1986)

Chapter Two: Nonequilibrium carrier dynamics in superconductors

This chapter reviews theoretical studies on photoexcitation of superconductors. The presented theories describe the basic, nonequilibrium carrier dynamics, and involve the electron condensate (Cooper pairs), QPs and phonons. They are the basis for our understanding of the measured photoresponse in the nanostructured F/S bilayers.

2.1 Optical photoexcitation of superconductors

The superconducting state is an ordered state of the conduction electrons of the metal. The order is in the formation of loosely associated pairs of electrons. The electrons are ordered at temperatures below T_c , and they are disordered above T_c [1]. The nature and origin of the ordering was explained by the BCS theory [2], which quantitatively predicts the basic electronic and magnetic properties of superconductors. The carriers in the superconducting system are pairs of electrons near the Fermi surface with the opposite momentum and spins. The Cooper pairs are formed through an electron-phonon exchange mechanism. Unlike single electrons, which are fermions and must obey the Pauli exclusion principle and follow the Fermi-Dirac energy distribution function, Cooper pairs act like bosons and condense

into the same energy level. The pairs have a certain binding energy per electron, Δ . An unpaired electron cannot exist in the superconducting ground state. To break a Cooper pair, the energy of 2Δ is required since an electron excited out of the superconducting ground state must pull its partner out too [2]. The superconducting state, therefore, has an energy gap between the normal state and superconducting electron state, analogous to the energy gap E_g between the valence band and conduction band in semiconductors, as shown in Fig. 2.1.

When subjected to photon energies $\hbar\omega \geq E_g$, electrons in a semiconductor will be excited across the gap resulting in the creation of electron-hole pairs [see Fig. 2.1(a)]. A similar situation occurs in superconductors, as illustrated in Fig. 2.1(b), where photons with $\hbar\omega \geq 2\Delta$ break Cooper pairs and transfer electrons high up into the continuum of excited states. These excitations are often referred to as QP excitations. They can have electron-like or hole-like properties. Meanwhile, two QPs can readily recombine to form a Cooper pair and emit a phonon with energy of 2Δ .

The energy gap is predicted by the BCS theory to be proportional to the T_c of the superconductor, and is expressed as

$$E_g(0) = 2\Delta(0) = 3.528k_B T_c, \quad (2.1)$$

where $2\Delta(0)$ is the energy gap at 0 K and k_B is the Boltzmann's constant. The 2Δ gap is a function of temperature. It has maximum value at 0 K, and decreases gradually to zero as the temperature is increased to T_c [see Fig. 2.2]. Finally, from the BCS theory one can derive a very simple expression for T_c as

$$T_c = 1.13 \hbar \omega_D \exp(-1/N_n(E_F)V/k_B), \quad (2.2)$$

where $\hbar \omega_D$ is the electron distribution energy range near the Fermi energy. When it is associated with characteristic phonon energy, the frequency ω_D is denoted as a characteristic phonon frequency, namely, the Debye frequency. $N_n(E_F)$ is the density of states of the non-interacting electrons. V is the attractive interaction energy.

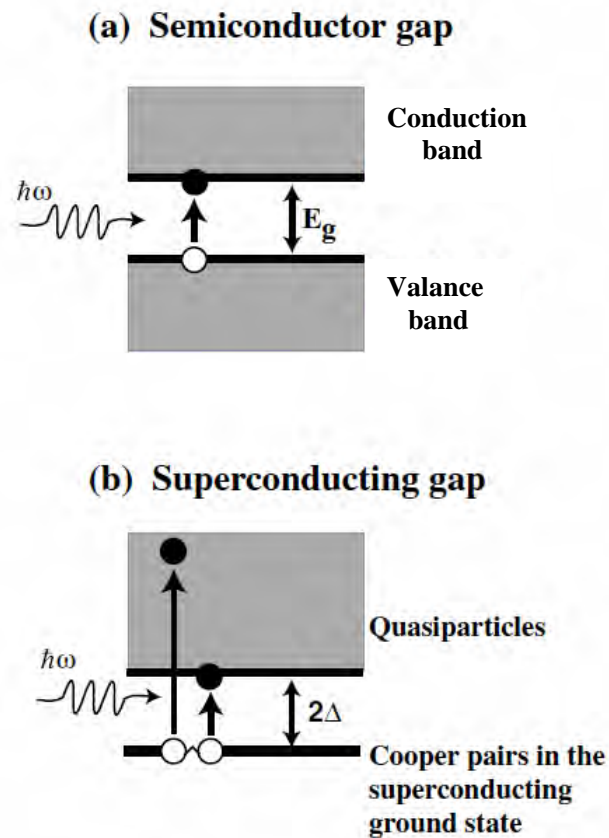


Figure 2.1: Simplified energy band diagrams of semiconductors (a) and superconductors (b). Energies $\hbar \omega \geq E_g$ can create electron-hole pairs in a semiconductor, or break Cooper pairs in a superconductor to create highly excited electrons if $\hbar \omega \geq 2\Delta$.

In a superconductor at temperature above 0 and below T_c , some of the electrons are not paired and follow the Fermi-Dirac distribution, thus, the electron

gas in it consists of two systems: paired electrons or Cooper pairs, and unpaired electrons or QPs.

Superconductor subjected to optical excitation ranging from the ultraviolet to well beyond the infrared with energies $\hbar\omega \geq 2\Delta$ will result in Cooper pairs being broken and QPs form. This is mentioned because of its relevance to applying superconductors to sensitive, broadband optical detectors.

The energy-relaxation time constants of excitations in thin and ultrathin nanostructure films of both the LTSs and HTSs materials are in the picosecond range, indicating that superconducting detectors exhibit the intrinsic response/counting rate in the GHz range. The overall photoresponse dynamics of superconductors and their recovery into the equilibrium state after photon absorption depends on a complex energy cascade, involving Cooper-pair breaking, QP recombination, and phonon interactions [3]. Understanding nonequilibrium QP dynamics in superconductors exposed to external excitations is the essential part for the superconducting theoretical research and experimental applications. For a femtosecond laser pulse excited superconductor, there is instantaneous formation of hot carriers in femtoseconds range. Subsequently, the immediate thermalization via electron-electron ($e-e$) and electron-phonon ($e-ph$) interactions leads the system reaching the state near the Fermi energy within several tens or hundred femtoseconds. Further QP relaxation and recombination dynamics can be studied by the method of measuring femtosecond laser pulse photoexcitation-induced time-domain changes in optical reflectivity (or transmissivity). Also, the nonequilibrium

QP relaxation dynamics can be studied by using an optical-pulse excitation of current-biased microbridges samples and then measuring an induced transient voltage signal. This is so-called photoimpedance studies. It allows for direct verification of applicability of a given material/structure for new type of photodetectors. We will discuss more details about these two experimental methods in Chapter 3.

From the theoretical research point of view, the dynamics of the nonequilibrium superconductivity is most often analyzed by means of two phenomenological approaches, the 2-T and RT models. In the following section, some of the useful expressions required for the two modelings will be summarized. Next, we will introduce our own extension of the 2-T model, namely, 3-T model.

2.2 Thermodynamics of the superconducting state

When we treat superconductivity on a macroscopic scale, by means of a rigorous application of the general laws of thermodynamics, one can reach a deep understanding of the properties of the superconducting state. This leads us to the Ginzburg-Landau theory [4], which was developed in the early 1950s. It serves for the description of conventional as well as unconventional superconductors.

In the Fermi-Dirac distribution function:

$$f(E, T) = \frac{1}{1 + \exp(E / k_B T)} \quad , \quad (2.3)$$

E is the excitation energy, which can be expressed as

$$E = [2\Delta(T)^2 + \varepsilon^2]^{1/2} \quad , \quad (2.4)$$

where ε is the QP kinetic energy and $\Delta = \Delta(T)$ is defined by BCS relation (2.1).

$$\frac{1}{N(0)V_{ep}} = \int_0^{\hbar\omega} \frac{\tanh \frac{1}{2k_B T} (\varepsilon^2 + \Delta^2)^{1/2}}{(\varepsilon^2 + \Delta^2)^{1/2}} d\varepsilon \quad , \quad (2.5)$$

where V_{ep} is electron-phonon coupling strength. Thus, the temperature-dependent thermal QP concentration $n_q(T)$ and energy $E_q(T)$ can be calculated by

$$n_q(T) = 4N(0) \int_0^{\infty} f(E, T) d\varepsilon \quad , \quad (2.6)$$

$$E_q(T) = 4N(0) \int_0^{\infty} E f(E, T) d\varepsilon \quad , \quad (2.7)$$

where $N(0)$ is the electron density of states at the Fermi level.

In the Bose-Einstein distribution function:

$$n(\omega) = [\exp(\hbar\omega / k_B T) - 1]^{-1} \quad (2.8)$$

the thermal 2Δ -phonon concentration $N_\omega(T)$ and energy $E_\omega(T)$ could be calculated from

$$N_\omega(T) = \nu \int_{2\Delta(T)}^{\omega_D} F(\omega) n(\omega) d\omega \quad (2.9)$$

$$E_\omega(T) = \nu \int_{2\Delta(T)}^{\omega_D} \hbar\omega F(\omega) n(\omega) d\omega \quad (2.10)$$

where ν is the ion density and $F(\omega)$ is the Debye phonon density of states:

$$F(\omega) = \frac{9\omega^2}{\omega_D^3} \quad (2.11)$$

Kaplan *et al.* derived expressions for the Cooper-pair breaking and recombination times by using the Eliashberg formulation $\alpha^2 F(\Omega)$, which summarizes the e - ph interaction [5,6]. The pair-breaking by phonons time τ_β is given by Kaplan *et al.* as

$$\tau_\beta^{-1}(\omega) = \frac{4\pi N(0)\alpha^2(\Omega)}{\hbar N} \times \left[\int_{\Delta}^{\omega-\Delta} d\Omega \frac{d\Omega}{[\omega^2 - \Delta]^2} \operatorname{Re} \left[\frac{\Omega(\omega - \Omega) + \Delta^2}{[(\omega - \Omega)^2 - \Delta^2]^{1/2}} \right] [1 - f(\Omega) - f(\omega - \Omega)] \right] \quad (2.12)$$

and the QP recombination time τ_R is

$$\tau_R^{-1}(\omega) = \frac{2\pi}{\hbar Z_1(0)[1-f(\omega)]} \times \left[\int_{\omega+\Delta}^{\infty} d\Omega \alpha^2 F(\Omega) \operatorname{Re} \left[\frac{\Omega - \omega}{[(\Omega - \omega)^2 - \Delta^2]^{1/2}} \right] \left(1 + \frac{\Delta^2}{\omega(\Omega - \omega)} \right) [n(\Omega) + 1] f(\Omega - \omega) \right], \quad (2.13)$$

where $Z_1(0)$ is renormalization function. In Eqs. (2.12) and (2.13), without losing the physical picture, the Debye approximation of Eliashberg function⁵

$$\alpha^2 F_D(\Omega) = b\Omega^2 \quad (2.14)$$

is used to simplify the calculations.

2.3 Rothwarf-Taylor model

The RT model introduced in 1967 is most applicable for describing the superconducting state's carrier dynamics when the temperature is maintained well below T_c [7]. At such temperatures, most of electrons in a superconductor near the Fermi surface are combined into Cooper pairs and occupy the single quantum condensate ground state. The superconducting ground state is separated from the QPs energy levels by a superconducting energy gap 2Δ . The fully opened energy gap at the Fermi surface significantly modifies the carrier dynamics upon optical excitation.

In the R-T phenomenology, the excited state is characterized by number density rather than the nonequilibrium energy distribution function. It describes the dynamics of excited QPs n_q and phonons N_ω , which have enough energy to break Cooper pairs. As schematically shown in Fig. 2.2, when light is incident on a superconductor, photons are absorbed by Cooper pairs, breaking the pairs and creating highly excited, hot electrons (QPs). Subsequently, these electrons lose their energy via $e-e$ scattering, followed by $e-ph$ interaction [Fig. 2.2 (a)]. Next, QPs recombine back to form Cooper pairs via emission of the so-called 2Δ -phonons, i.e., phonons with the energy of at least 2Δ [Fig. 2.2 (b)]. Obviously, the 2Δ -phonon has enough energy to break another Cooper pair and form two new QPs [Fig. 2.2 (c)]. This nonlinear pair formation and breaking process results in the so-called “phonon bottleneck” mechanism that continues until all phonons reach equilibrium either via

anharmonic decay to low-energy phonons, or by escaping out of the region of interest [Fig. 2.2 (d)] [8].

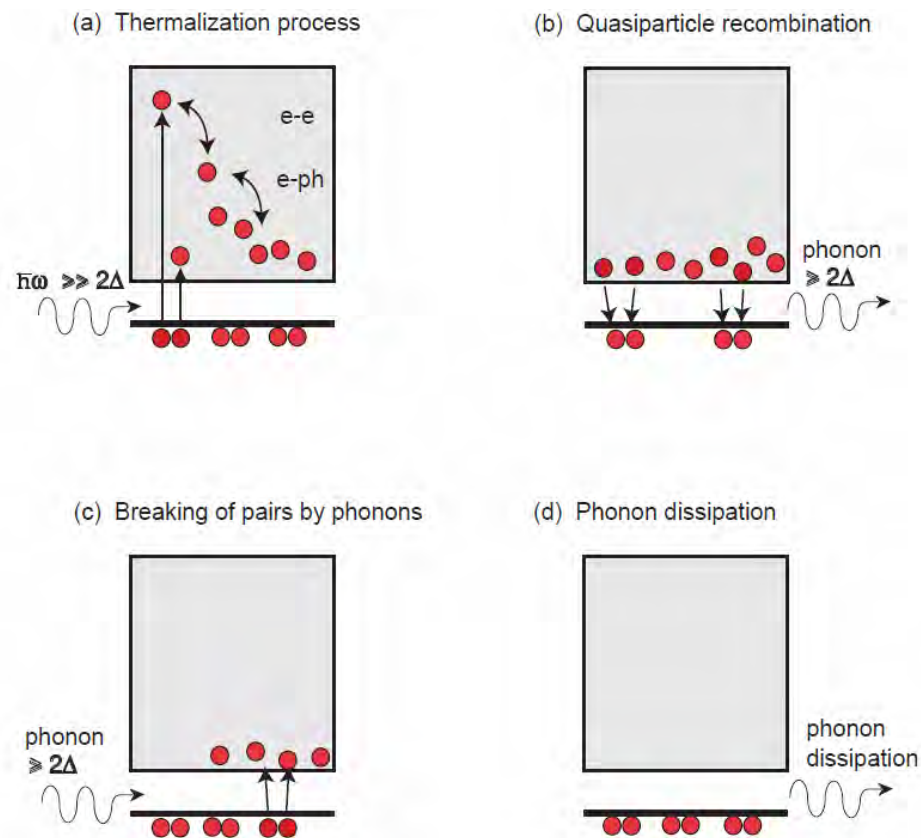


Figure 2.2 Schematics of carrier dynamics in the superconducting state under optical excitation.

QPs recombination into Cooper pairs and the associated “photon bottleneck” are the intrinsic factors limiting the superconducting recovery dynamics. The presence of the phonon bottleneck effectively slows down the recovery process. Quantitatively the process can be modeled by the two coupled, time-dependent nonlinear differential RT equations [7]:

$$\frac{dn_q}{dt} = I(t) - Rn_q^2 + 2\beta N_\omega \quad , \quad (2.15)$$

$$\frac{dN_\omega}{dt} = \frac{Rn_q^2}{2} - \beta N_\omega - (N_\omega - N_{\omega T})\tau_{es}^{-1} \quad , \quad (2.16)$$

where n_q and N_ω , as we mentioned before, are QP and 2Δ -phonon concentrations respectively, R and β are QP recombination and pair-breaking rates respectively, τ_{es} is the phonon escape time, $N_{\omega T}$ is the thermal equilibrium concentration of 2Δ -phonons, and $I(t)$ is the excitation pulse.

Note that following relation must hold to satisfy equilibrium conditions:

$$Rn_{qT}^2 = 2\beta N_{\omega T} \quad , \quad (2.17)$$

and τ_{es} is related to R through

$$\tau_{es} = 1 / Rn_{qT} \quad , \quad (2.18)$$

where n_{qT} is the thermal equilibrium QP concentration.

The RT equations are generally used to analyze the response of nonequilibrium superconductors, however, more extensive modeling can be done through the kinetic equation approach in which QP and phonon kinetic equations govern the energy distributions of QPs and phonons [9].

2.4 Two-temperature model

When a superconductor is maintained at temperature close to T_c , the signature of 2Δ is very weak (concentration of Cooper pairs is low) and under weak perturbation, we can use the normal metal approach: assume that electrons and phonons are described in terms of their energy distributions and assign two different temperatures T_e and T_{ph} to the electron and phonon subsystems respectively. Next we can describe the nonequilibrium thermalization process of a superconductor after excitation by the classical 2-T model, first developed by Kaganov, Lifshitz, and Tanatarov [10, 11]. We need to stress that under T close to T_c condition, RT model can be linearized and the resulting equations become equivalent to the 2-T model.

The 2-T model is qualitatively illustrated in Figure 2.3. Firstly, when an ultrashort (typically < 1 ps) laser pulse is incident on the superconducting film sample, photon energy is absorbed in the electron subsystem. Within the optical pulse duration, Cooper pairs are broken, highly excited electrons are produced, and after the initial almost instantaneous e - e scattering (characteristic time τ_T is on the order of femtoseconds), the Fermi distribution has been re-established. The above initial stage relaxation is actually identical to that described in the case of the RT model. Next, we use average energies of electron and phonon subsystems, instead of their concentrations. The average energy of the electron subsystem represented by T_e , as compared to the sample bath temperature T_b , increases according to its heat capacity C_e . The electrons relax, interacting with phonons, on a time scale of the

picosecond level represented by τ_{e-ph} . The excess energy transfers from the electron subsystem to phonon subsystem increases the phonon subsystem temperature T_{ph} , according to its heat capacity C_{ph} . There is also a reverse $ph-e$ energy transfer, typically characterized by characteristic time τ_{ph-e} , which is much slower than τ_{e-ph} , as it is coupled via a balance equilibrium condition equation $C_{ph}\tau_{e-ph} = C_e\tau_{ph-e}$. Finally, all the pump excitation energy transferred to phonons drains away from the superconducting film sample by anharmonic decay and/or heat transfer to the substrate. The latter process is called the phonon-escape, on a time scale τ_{es} , which varies from tens of picoseconds to nanoseconds and even microseconds, since it depends on the thickness of the superconducting material and the thermal transmissivity of the film-substrate interface [12].

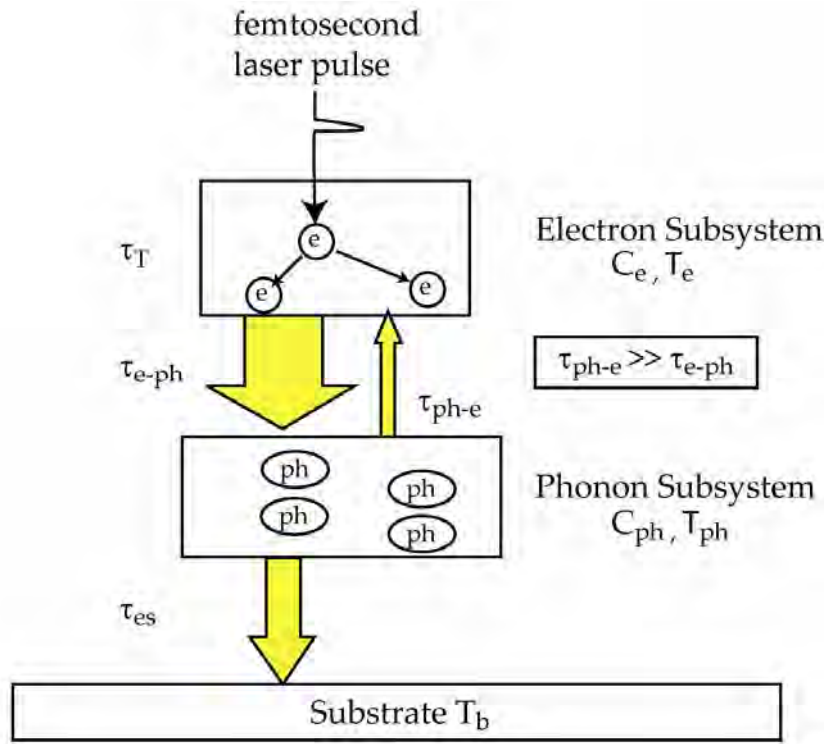


Figure 2.3 Energy flow and its relaxation time among the electron and phonon subsystems and the substrate in the 2-T model.

The energy balance between the electron and phonon subsystems in 2-T model can be present as two coupled, time-dependent, energy-balanced, differential equations:

$$C_e \frac{dT_e}{dt} = I(t) - \frac{C_e}{\tau_{e-ph}} (T_e - T_{ph}) \quad (2.19)$$

$$C_{ph} \frac{dT_{ph}}{dt} = \frac{C_{ph}}{\tau_{ph-e}} (T_e - T_{ph}) - \frac{C_{ph}}{\tau_{es}} (T_{ph} - T_b) \quad (2.20)$$

where $I(t)$ represents the laser source.

The 2-T model was derived based on the assumption, that right after the excitation process, electrons and phonons are described by the equilibrium Fermi-Dirac and Bose-Einstein distribution functions, respectively, but at different temperatures [13]. In the case of most conventional pump-probe experiments on metals at room temperature and high excitation powers, the balance equation can be written as

$$\frac{C_e}{\tau_{e-ph}} = \frac{C_{ph}}{\tau_{ph-e}} = \frac{3\hbar\lambda\langle\omega^2\rangle\gamma}{\pi k_b} \quad , \quad (2.21)$$

where

$$\lambda\langle\omega^2\rangle = 2\int_0^\infty \frac{\alpha^2 F(\omega)}{\omega} \omega^2 d\omega \quad , \quad (2.22)$$

where $\lambda\langle\omega^2\rangle$ is second moment of $\alpha^2 F(\omega)$, resulting in $\tau_{e-ph} \propto T_e$, at high temperatures. However at low temperatures, $\tau_{e-ph} \propto T_e^3$, which was pointed out by the authors of the 2-T model [13]. Therefore, at low temperatures, a slow electron thermalization dynamics is expected, which has been verified by K. H. Ahn *et al.* [14] in some metals already.

In our later application of the 2-T equations to the analysis of our experimental data of photoresponse of F/S nano-bilayers, the C_e and C_p are estimated using classical expressions [1].

$$C_e = \gamma T \quad , \quad (2.23)$$

$$C_{ph} = \beta_3 T^3 \quad , \quad (2.24)$$

where the values for γ and β_3 are the Sommerfield constant and the phonon specific heat constant, respectively.

From Fig. 2.3 we can see that in the 2-T model the last process is the phonon cooling section. The governing mechanism is phonon escape to substrate in the case of a thin film, which is physically identical to the RT-model's last process. It is out-diffusion of electrons and phonons in bulk samples or thick films cases.

The phonon escape characteristic time τ_{es} can be derived by the phonon transparency at the film- substrate interface:

$$\tau_{es} = C_{ph} d R_B \quad , \quad (2.25)$$

where d is the film thickness and R_B is the thermal boundary resistance between the film and the substrate.

2.5 Three-temperature model

2-T model is good for describing the nonequilibrium thermalization process of a superconductor after photon excitation. However, in experiments we often observe a bi-exponential decay of the photoresponse signal (See Chap. 4 for details). From the physics point of view, in 2-T model, we assume the electron subsystem interacts with one phonon subsystem, which in practice is the acoustic phonon subsystem with the heat capacity, C_{ph} . Actually, one should take into account both optical phonons (Oph) and acoustical phonons (Aph) with separate heat capacities, C_{Oph} and C_{Aph} , respectively. This is what I introduced here: three temperature (3-T) model.

The 3-T model is illustrated in Fig. 2.4. Firstly, as before, when an ultrashort (typically < 1 ps) laser pulse is incident on the superconducting film sample, photon energy is absorbed in the electron subsystem. Within the optical pulse duration, Cooper pairs are broken, highly excited electrons are produced, and after the initial almost instantaneous $e-e$ scattering, the Fermi distribution has been re-established. As in the 2-T model, the average energy of the electron subsystem represented by T_e , as compared to the sample bath temperature T_b , increases according to its heat capacity C_e . Next, the electrons relax, interacting with optical and acoustical phonons simultaneously, on a time scale of the picosecond-level represented by τ_{e-Oph} and τ_{e-Aph} , respectively, and $\tau_{e-Oph} < \tau_{e-Aph}$. In the early stages of relaxation, the $e-Oph$ process is the most efficient one, while later QPs in a superconductor interact predominantly with Aph .

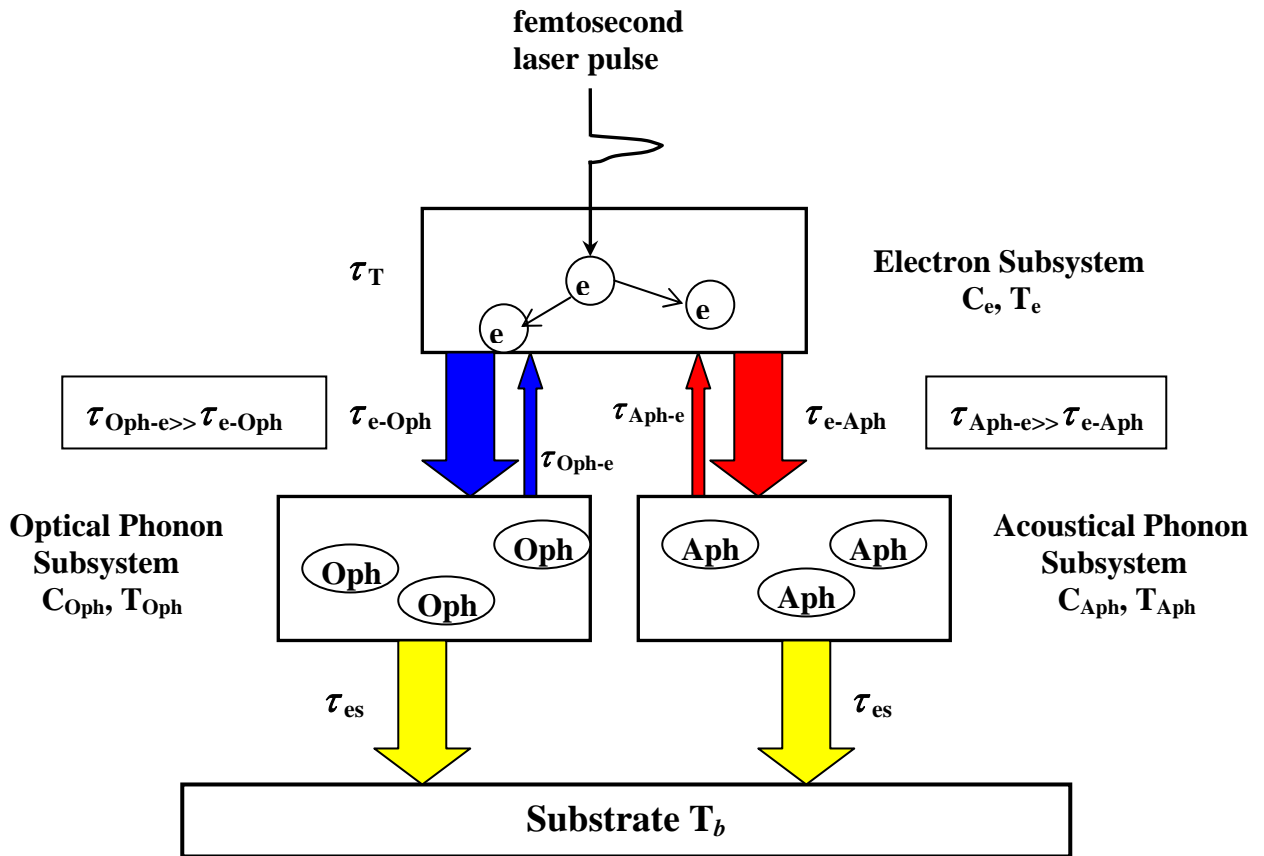


Figure 2.4 Energy flow among the electron subsystem, optical phonon subsystem and acoustical phonon subsystem in the 3-T model.

The excess energy transfers from the electron subsystem to the two phonon subsystems and increases their T_{Oph} and T_{Aph} , according to their C_{Oph} and C_{Aph} , respectively. There is also a reverse *Oph-e* and *Aph-e* energy transfer, typically characterized by characteristic times τ_{Oph-e} and τ_{Aph-e} , which are typically much longer than τ_{e-Oph} and τ_{e-Aph} respectively. Similar to the 2-T model's balance equation $C_{ph}\tau_{e-ph} = C_e\tau_{ph-e}$, in the 3-T model we have $C_{Oph}\tau_{e-Oph} = C_e\tau_{Oph-e}$ and $C_{Aph}\tau_{e-Aph} = C_e\tau_{Aph-e}$. Finally, again, as in the 2-T model, all the pump excitation energy

transferred to phonons drains away from the superconducting film sample by anharmonic decay and/or heat transfer to the substrate on a time scale τ_{es} , which varies from tens of picoseconds to nanoseconds and even microseconds.

We can use the following energy balanced, time dependent, differential equations to describe the 3-T model:

$$C_e \frac{dT_e}{dt} = I(t) - \frac{C_e}{\tau_{e-Oph}} (T_e - T_{Oph}) - \frac{C_e}{\tau_{e-Aph}} (T_e - T_{Aph}) \quad , \quad (2.26)$$

$$C_{Oph} \frac{dT_{Oph}}{dt} = \frac{C_{Oph}}{\tau_{Oph-e}} (T_e - T_{Oph}) - \frac{C_{Oph}}{\tau_{es}} (T_{Oph} - T_b) \quad , \quad (2.27)$$

$$C_{Aph} \frac{dT_{Aph}}{dt} = \frac{C_{Aph}}{\tau_{Aph-e}} (T_e - T_{Aph}) - \frac{C_{Aph}}{\tau_{es}} (T_{Aph} - T_b) \quad , \quad (2.28)$$

where $I(t)$ represents, as before, the laser source.

The numerical solution of the 3-T model, as well as its nice agreement with experimental data will be presented in Chap. 4.

2.6 Kinetic-inductive and resistive photoresponse

As we stressed in the previous chapter, after absorption of an optical photon with the energy $\hbar\omega \geq 2\Delta$, local nonequilibrium distributions of both QPs and phonons are created in a superconducting film. Spatially, this thermalization phase is characterized by formation and growth of a hotspot, a local nonsuperconducting (or superconductivity-suppressed) region inside a superconducting material [15].

There are two types of voltage response when photons excite a current biased superconducting microbridge: kinetic-inductive response and resistive response. In the first case, if an optically irradiated superconducting sample is of a micrometer size or larger and the flux of photons is weak, i.e., insufficient to generate enough overlapping hotspots completely ruin the superconductivity, the nonequilibrium superconducting and normal states coexist and we can observe the kinetic-inductive photoresponse, which is based on the inertiallike inductive response of a superconducting condensate [16]. Under optical irradiation, the kinetic inductance L_{kin} of a superconducting sample is determined by the nonequilibrium energy distribution function of QPs $f(\varepsilon)$ and by the value of Δ , and given as:

$$\frac{1}{L_{kin}} = \frac{\sigma_n}{\hbar} \int_{\Delta-\hbar\Omega}^{\Delta} d\varepsilon [1 - 2f(\varepsilon - \hbar\Omega)] \frac{\varepsilon(\varepsilon + \hbar\Omega) + \Delta^2}{\sqrt{(\Delta^2 - \varepsilon^2)}\sqrt{(\varepsilon + \hbar\Omega)^2 - \Delta^2}} \quad (2.29)$$

where σ_n is the normal-state conductivity and the integral is taken over an interval of energies $\hbar\Omega$ close to Δ [17, 18].

On the other hand, under strong optical irradiation, the superconducting sample switches into the resistive state and the observed voltage change $V_r(t)$ is described by

$$V_r(t) = I_b \frac{dR(T)}{dT} \Delta T(t) \quad , \quad (2.30)$$

where I_b is the bias current and $dR(T)/dT$ is taken over the resistance versus temperature $R(T)$ curve. This resistive response is bolometric and can be well described by Eq. (2.30) assuming $T(t)$ is the actual time varying temperature of the sample [19].

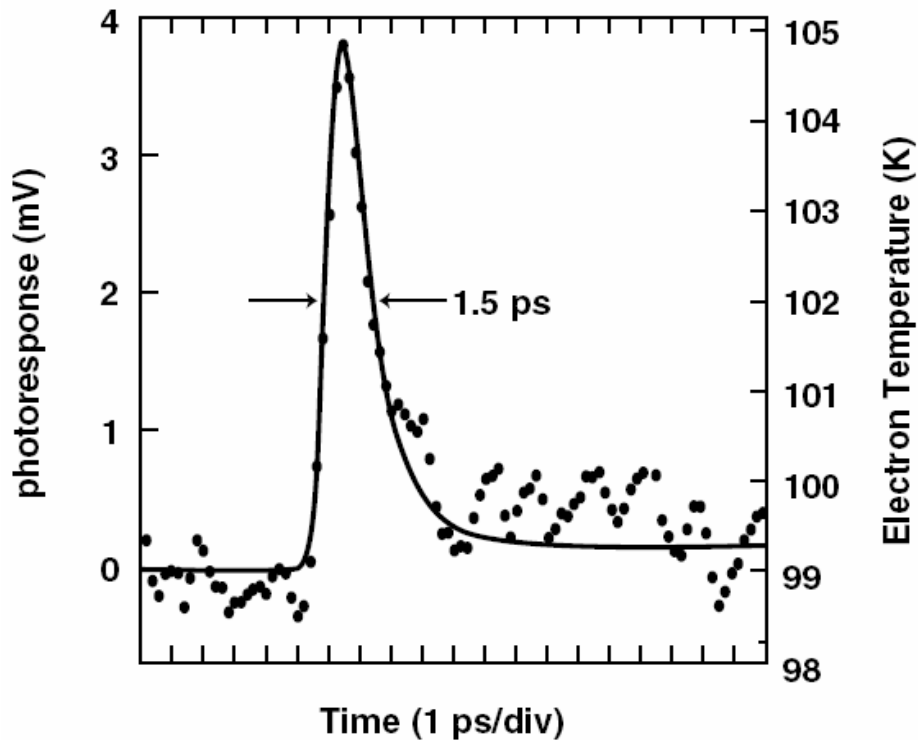


Figure 2.5 Measured photoresponse of a YBCO microbridge at $T = 80$ K when the bridge was biased in the resistive hot-spot state, and fitted with the nonequilibrium electron heating two-temperature photoresponse model [20].

In this thesis, we are predominantly interested in the nonequilibrium kinetic-inductive response, which shows faster response time as well as higher sensitivity. In the kinetic-inductive scenario, the studied sample remains all the time in the superconducting state. The inductance of a current-biased superconducting microbridge is modified by photoexcitation-induced QP population, or equivalently the increase of T_e . In the latter case, the solution of 2-T model equations allows us to calculate the L_{kin} through the following equation [21]:

$$L_{kin}(t) = \frac{1}{\epsilon_0 \omega_p^2} \frac{1}{f_{sc}} \frac{l}{wd} , \quad (2.31)$$

where ω_p is the plasma frequency of the superconductor and l , w , and d are the length, width, and thickness of the sample, respectively. f_{sc} is the superfluid fraction defined as $f_{sc} = 1 - (T_e/T_c)^2$. Accordingly, the change of L_{kin} of a current biased microbridge-type sample can be quite large and leads to a measurable voltage transient across the bridge, given by:

$$V_{kin} = I_b(dL_{kin} / dt) \quad (2.32)$$

By solving the R-T model equations, the number of QPs is directly calculated. f_{sc} comes naturally from its definition $f_{sc} = (1 - n_q)/N(0)$, where n_q is QP density and $N(0)$ is the electron density of states as we stated before. Therefore, L_{kin} can also be calculated from R-T model equations.

The kinetic inductive response was first identified by Hegmann *et al.* [22]. However, due to the long laser pulse width (100 ps FWHM), the fast e - ph relaxation process was not observed in that experiment and for our simulations f_{sc} was taken as $1 - (T_{ph}/T_c)^2$. The first intrinsic nonequilibrium kinetic inductive response was reported in our laboratory in 1995 [23]. The fast voltage transient with an FWHM of 1.5 ps was measured in a 100-nm-thick YBCO microbridge. In that kinetic inductive response measurement, the microbridge of YBCO was excited with femtosecond (~ 100 fs) laser pulses and measured with a cryogenic EO sampling system.

The measured nonequilibrium L_{kin} time-resolved voltage transients consisted of a picosecond bipolar response, followed by a fast-damped oscillation at the end of the bipolar shape. Later, Lidgren *et al.* studied the nonequilibrium resistive and kinetic inductive response in detail using the 2-T and R-T models [24]. A typical kinetic inductive response is shown in Fig. 2.6, with fitting curves using the R-T model equations.

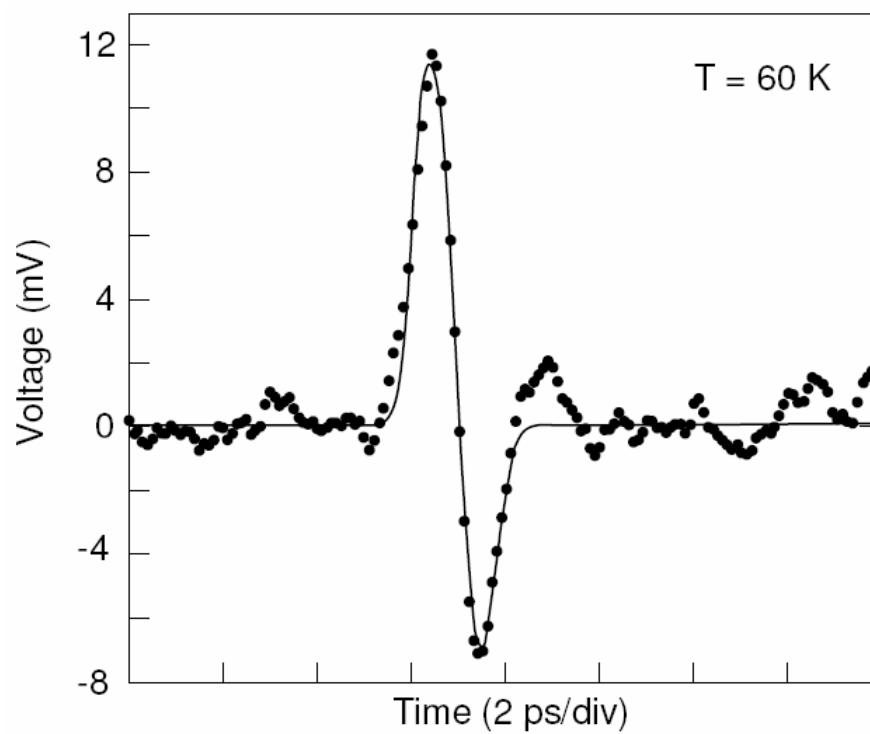


Figure 2.6 Measured kinetic inductive voltage photoresponse of a YBCO microbridge (solid dots) fitted using R-T model (solid line) at temperature below T_c [25].

References:

-
- ¹ C. Kittel. *Introduction to Solid State Physics*. 7th edition. (John Wiley and Sons, New York (1996).
- ² J. Bardeen, L. N. Cooper, and J. R. Schrieffer. Theory of superconductivity. *Phys. Rev.* 108, 1175 (1957).
- ³ G. P. Pepe, D. Pan, V. Pagliarulo, L. Parlato, N. Marrocco, C. De Lisio, G. Peluso, A. Barone, U. Scotti di Uccio, A. Casaburi, F. Tafuri, M. Khafizov, T. Taneda, and R. Sobolewski. Ultrafast Photoresponse of Superconductor/Ferromagnet Nano-Layered Hybrids. *IEEE Trans. Appl. Supercon.* 19, 376 (2009).
- ⁴ V. L. Ginzburg, L. D. Landau. *Zh. Eksp. Teor. Fiz.* 20, 1044 (1950).
- ⁵ S. B. Kaplan, C. C. Chi, D. N. Langenberg, J. J. Chang, S. Jafarey, and D. J. Scalapino. Quasiparticle and phonon lifetimes in superconductors. *Phys. Rev. B*, 14, 4854 (1976).
- ⁶ G M Eliashberg. *Soviet Physics JETP*, 11:696 (1960).
- ⁷ A. Rothwarf and B.N. Taylor, Measurement of recombination lifetimes in superconductors. *Phys. Rev. Lett.* 19, 27 (1967).
- ⁸ A. M. Kadin, *Introduction to Superconducting Circuits*. John Wiley & Sons Canada, Ltd. (1999).
- ⁹ J. J. Chang and D. J. Scalapino. Kinetic-equation approach to nonequilibrium superconductivity. *Phys. Rev. B*, 15, 2651 (1977).

-
- ¹⁰ S. B. Kaplan, C. C. Chi, D. N. Langenberg, J. J. Chang, S. Jafarey, and D. J. Scalapino. Quasiparticle and phonon lifetimes in superconductors. *Phys. Rev. B* 14, 4854, (1976).
- ¹¹ N. Perrin and C. Vanneste. Response of superconducting films to a periodic optical irradiation. *Phys. Rev. B* 28, 5150 (1983).
- ¹² T. Taneda, G.P. Pepe, L. Parlato, A.A. Golubov, and R. Sobolewski. Time-resolved carrier dynamics and electron-phonon coupling strength in proximized weak ferromagnet-superconductor nanobilayers. *Phys. Rev. B* 15, 174507 (2007).
- ¹³ M I Kaganov, I M Lifshitz, and L V Tanatarov. Relaxation between electrons and the crystalline lattice. *Soviet Physics JETP*, 4, 173 (1957).
- ¹⁴ K. H. Ahn, T. Lookman, A. Saxena, and A. R. Bishop. Electronic properties of structural twin and antiphase boundaries in materials with strong electron-lattice couplings. *Phys. Rev. B*, 71, 212102 (2005)
- ¹⁵ A. M. Kadin and M. W. Johnson. Nonequilibrium photon-induced hotspot: A new mechanism for photodetection in ultrathin metallic films. *Appl. Phys. Lett.* 69, 3938. (1996).
- ¹⁶ N. Bluzer. Temporal relaxation of nonequilibrium in Y-Ba-Cu-O measured from transient photoimpedance response. *Phys. Rev. B* 44, 10222 (1991).
- ¹⁷ A. Verevkin, J. Zhang, R. Sobolewski, A. Lipatov, O. Okunev, G. Chulkova, A. Korneev, K. Smirnov, and G. N. Gol'tsman, and A. Semenov. Detection Efficiency of Large-Active-Area NbN Single-Photon Superconducting Detectors in the Ultraviolet to Near-Infrared Range. *Appl. Phys. Lett.* 80, 817 (2002).

-
- ¹⁸ D. Pan, G. P. Pepe, V. Pagliarulo, C. De Lisio, L. Parlato, M. Khafizov, I. Komissarov, and Roman Sobolewski. Layered ferromagnet/superconductor heterostructures: nonequilibrium quasiparticle dynamics and photodetector applications. *Physical Review B*, 78, 174503 (2008).
- ¹⁹ G. L. Carr, M. Quijada, D. B. Tanner, C. J. Hirschmug, G. P. Williams, S. Etemad, B. Dutta, F. DeRosa, A. Inam, T. Venkatesan, and X. Xi. Fast bolometric response by high T_c detectors measured with subnanosecond synchrotron radiation. *Appl. Phys. Lett.* 57, 2725 (2000).
- ²⁰ C. Williams, Ph.D. Thesis. University of Rochester, Rochester, NY. (2001).
- ²¹ C. J. Stevens and D.J. Edwards. Photomixing receiver using the kinetic inductive effect in high T_c superconductors. *Electronics Lett.* 37, 23, 1420 (2001).
- ²² F. A. Hegmann and J. S. Preston. Origin of the fast photoresponse of epitaxial $\text{YBa}_2\text{Cu}_3\text{O}_{7-\delta}$ thin films. *Phys. Rev. B.*, 48(21):285 (1993).
- ²³ F. A. Hegmann, D. Jacobs-Perkins, C.-C. Wang, S. H. Moffat, R. A. Hughes, J. S. Preston, M. Currie, P. M. Fauchet, T. Y. Hsiang, and R. Sobolewski. Electro-optic sampling of 1.5-ps photoresponse signal from $\text{YBa}_2\text{Cu}_3\text{O}_{7-\delta}$ thin films. *Appl. Phys. Lett.*, 67:285-287. (1995).
- ²⁴ M. Lindgren, M. Currie, C. A. Williams, T. Y. Hsiang, P. M. Fauchet, R. Sobolewski, S. H. Moffat, R. A. Hughes, J. S. Preston, and F. A. Hegmann. Ultrafast photoresponse in microbridges and pulse propagation in transmission lines made from high- T_c superconducting $\text{YBa}_2\text{Cu}_3\text{O}_{7-\delta}$ thin films. *IEEE J. Sel. Top. Quantum Electron.*, 2, 668. (1996).

²⁵ M. Lindgren, M. Currie, C. Williams, T. Y. Hsiang, P. M. Fauchet, and R. Sobolewski. Intrinsic Photoresponse Times of Y-Ba-Cu-O Superconducting Photodetectors. *Appl. Phys. Lett.*, 74, 853 (1999).

Chapter Three: Ferromagnet/Superconductor nano-bilayers: sample characterization, and transient photoresponse experimentation

In this chapter, the F/S nano-bilayers samples fabrication process and characterization are explained. Principles and experimental setups for both the transient reflectivity and time-resolved photoimpedance experiments are presented.

3.1 Nano-bilayers fabrication and patterning

Weak F/S proximity bilayers have been fabricated for basic physics studies concerning the ultrafast carrier dynamics in layered materials. The samples include F/S hetero-structures formed by a LTS (Nb and NbN) with a NiCu overlayer, and a HTS (YBCO) covered by NiCu/Au and manganite (LSMO) overlayers [1]. The schematic of the bilayer is shown in Fig. 3.1. In the figure, NiCu alloy and Nb represent the F and S layers, respectively. All the F/S bilayers samples were fabricated by our collaborators from the University of Naples, Italy, in the group of Professor G. P. Pepe.

Thin films of Nb and $\text{Ni}_{0.48}\text{Cu}_{0.52}$ weak-ferromagnetic alloy have been deposited by DC magnetron sputtering in two separate vacuum systems to avoid contamination. 60-nm-thick to 70-nm-thick base Nb layers were sputtered at a base pressure of 1×10^{-7} Torr on chemically cleaned Corning glass substrates. The substrate

size was $10 \times 10 \times 1 \text{ mm}^3$. The sputtering power density and deposition rate were 10 W/cm^2 and 2.2 nm/s , respectively. Next, the Nb samples were inserted into a NiCu deposition system, where their surface was first pre-cleaned for 30 s using ion-beam etching at an argon pressure in $\sim 10^{-3} \text{ Pa}$ at a rate of about 0.2 nm/s . Afterward $\text{Ni}_{0.48}\text{Cu}_{0.52}$ films were sputtered at a rate of 1.5 nm/s using a power density of 10 W/cm^2 . The NiCu thickness of the sample used for later photodetection experiments varied from 6 nm to 21 nm.

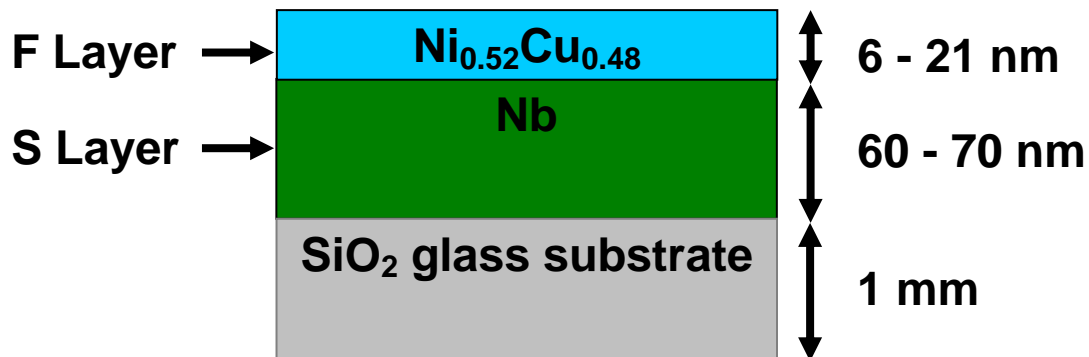


Figure 3.1: Schematics of the F/S nano-bilayer.

YBCO films, 100-nm thick and c-axis oriented, were deposited by DC magnetron sputtering on SrTiO_3 substrates at $T = 950 \text{ }^\circ\text{C}$. The sputtering power density and the deposition rate were 100 W/cm^2 and 3 nm/s , respectively. The films were annealed at $T = 500 \text{ }^\circ\text{C}$, and, subsequently, covered with a sputtered Au buffer layer ($\sim 10\text{nm}$ to 20nm thick), deposited in order to reduce the diffusion of O_2 outside the YBCO layer surface. Afterward, the samples were moved into the $\text{Ni}_{0.48}\text{Cu}_{0.52}$ dedicated sputtering system, a surface of Au was cleaned at a rate of about 0.2 nm/s

by soft Ar ion beam, and finally coated with 6-nm-thick to 21-nm-thick $\text{Ni}_{0.48}\text{Cu}_{0.52}$ films deposited as described in the previous subsection.

The deposition of YBCO/LSMO bilayers was carried out in a modular system used for oxide depositions and analyses named Modular system for Oxide Deposition and Analyses (MODA) at the University of Naples. The MODA unit is a multi-chamber, ultrahigh-vacuum system, which includes a base chamber (pressure in the 10^{-7} -Pa range) devoted to pulsed laser deposition (PLD), assisted by a reflection high-energy electron diffraction (RHEED) system operating up to 0.5×10^2 Pa of O_2 , and three analytical chambers (pressure in the $\sim 10^{-11}$ -mbar range) equipped with UV/x-ray photoemission spectroscopy (UPS/XPS), spot profile analysis low-energy electron diffraction (SPA-LEED), and the scanning force and scanning tunneling microscopes (AFM/STM).

The KrF excimer laser ($\lambda = 248$ nm) was operated at 1-2 Hz repetition rate and the effective fluence was 2 J/cm^2 at the target for PLD deposition. The (001) SrTiO_3 substrates were held at 800°C , in an O_2 atmosphere at 0.25×10^2 Pa. Under these conditions, YBCO grew at a rate of about one monolayer per 30 laser shots. The deposition of LSMO took place under the same conditions, without breaking the vacuum. The cooling of YBCO/LSMO samples included a prolonged exposure to the O_2 atmosphere at 500°C to promote the full oxidation of YBCO through the LSMO cap layer. A collection of samples, fabricated for our studies, included 100-nm-thick pure YBCO and LSMO films (used as the reference) and bilayers with 10-, 35-, and 100-nm capping of LSMO over the 100-nm-thick YBCO base.

The 100-nm-thick NbN films were deposited by DC reactive magnetron sputtering on single-crystal MgO (100) substrates in a mixture of Ar (85%) and N₂ (15%) gases at an ambient temperature and at a sputtering pressure of 1.6×10^{-1} Pa. The background pressure was less than 7×10^{-7} Pa and the sputtering power was 440 W, corresponding to a voltage and current discharge of 358 V and 1.2 A, respectively.

3.2 Structural and electrical characterization of bilayers

The properties of F/S bilayers were characterized in terms of film thickness, chemical composition, crystallinity, surface roughness, critical current I_c , and T_c . The film thickness was measured by Surface Profile Measuring System and also by Transmission Electron Microscope (TEM). The chemical composition of the NiCu alloy was examined by Inductively Coupled Plasma Atomic Emission Spectroscopy (ICP-AES) and Energy-Dispersive X-ray spectroscopy (EDX). The crystallinity was observed with TEM image and selected area diffraction (SAD) pattern. The surface roughness was measured by Atomic Force Microscope (AFM). The I_c and T_c were measured by using Josephson junctions and by resistance with various temperatures, respectively.

Fig. 3.2 is taken from T. Taneda *et al.* [2] and shows a transmission electron microscope TEM picture of sample NiCu (6 nm)/Nb (60 nm). EDX point measurements were performed on the five points (from No. 1 to No. 5). The points No. 1 and No. 5 were in the NiCu and Nb layers, respectively, while the points No. 2

to No. 4 were at the interface of NiCu and Nb layers. We note that the Nb film is polycrystalline, while the NiCu is either amorphous or polycrystalline with a grain size <1 nm. The NiCu/Nb interface is almost atomically flat and very sharp. The atomic composition of the resulting films was measured by EDX and demonstrated that the composition of the deposited NiCu alloy was reasonably close to that of the target point 1 in Fig. 3.2, although we observed a somewhat higher concentration of Ni close to the F/S interface points 2, 3, and 4, and a partial diffusion of the Ni on the Nb side point 5. The detailed compositions at indicated points, expressed in terms of atomic percentages of both Ni and Cu, are listed in Table 3-1.

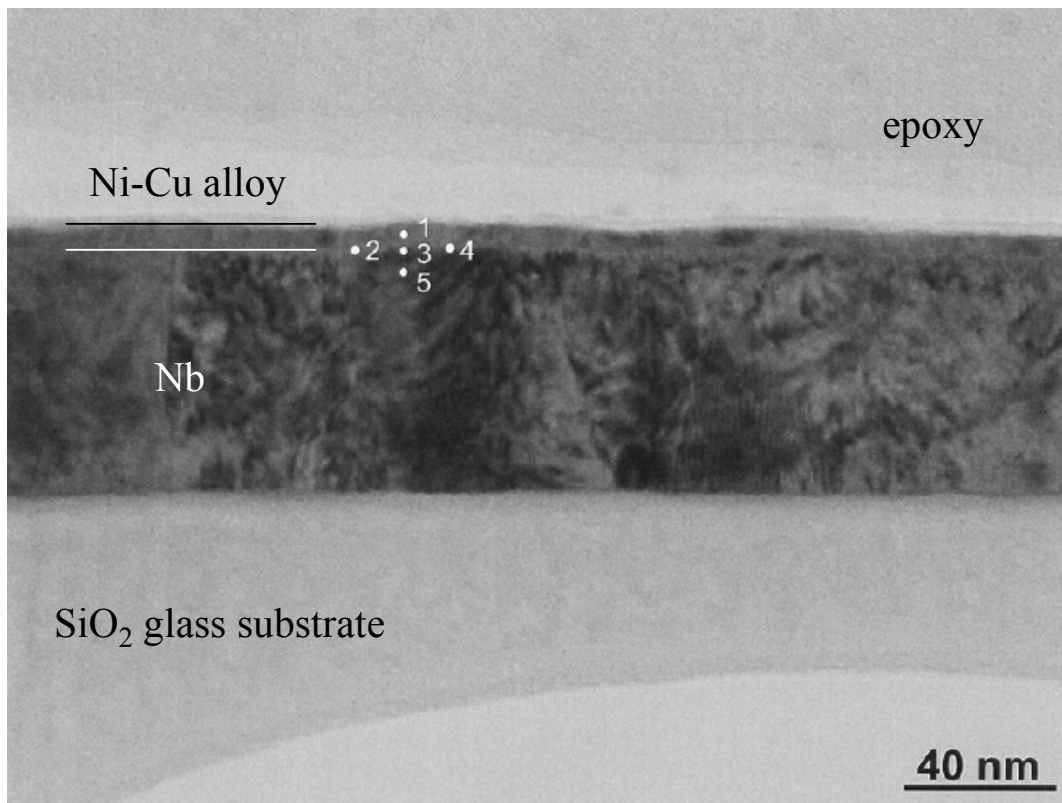


Figure 3.2: TEM image of the cross section of NiCu (6 nm)/Nb (60 nm) bilayer film [2].

Table 3.1 Summarization of the concentration of Ni and Cu at the five points, setting the sum of those concentration to be 100 atomic % [2].

Position	NiCu layer		NiCu/Nb interface		Nb layer
Point #	1	2	3	4	5
Ni	52.7	73.2	72.9	62.6	54
Cu	47.3	26.8	27.1	37.4	46
					(Atomic %)

Low-temperature magnetization tests performed for plain $\text{Ni}_{0.48}\text{Cu}_{0.52}$ films showed a Curie temperature of $T_{Cf} \sim 30$ K and a spontaneous moment per atom $\mu_0 = 0.06 \mu_B/\text{atom}$ at $T = 4.2$ K; both values are typical for a weak ferromagnetism [3]. The roughness, measured by AFM analyses, was found to be much lower than any investigated F thicknesses (roughness $\ll 6$ nm). The critical temperature of pure Nb was $T_c = 8.9$ K, while $T_c = 8.5$ K for NiCu (21 nm)/Nb (70 nm). The T_c of the Nb layer was slightly suppressed due to the presence of the ferromagnetism in the NiCu layer as we expected.

Figure 3.3 presents our critical current density J_c dependences for both pure Nb (100 nm) and NiCu (21 nm)/Nb (70 nm) microbridges on temperature. We note that contrary to the most recent work of Angrisani Armenio *et al.* [4], we observe a strong enhancement of J_c for the F/S bilayer as compared to the pure Nb microbridge. The pinning of vortices in proximized superconducting bilayers represents an interesting field of investigation, and different physical mechanisms have been proposed for the explanation of the J_c enhancement observed in F/S structures [5]. Our F layer consists of a weak ferromagnet instead of Permalloy as in Angrisani Armenio's work; thus, we expect a homogeneous vortex pinning, which should be

enhanced for NiCu/Nb bridges due to the presence of the NiCu overlayer. In addition, as was shown in Fig. 3.2, there is diffusion of NiCu into Nb, which also must increase pinning. The latter is clearly visible in Fig. 3.3 (inset), which presents the current-voltage (I - V) characteristics of both microbridges measured at 8 K in a semilogarithmic scale. Both curves exhibit behavior that is typical of a long superconducting constriction with a wide jump to the fully resistive state, but in the case of the Nb bridge, we can clearly identify a well-developed flux-flow region at low voltages, which is essentially missing in the NiCu/Nb sample due to a much stronger pinning.

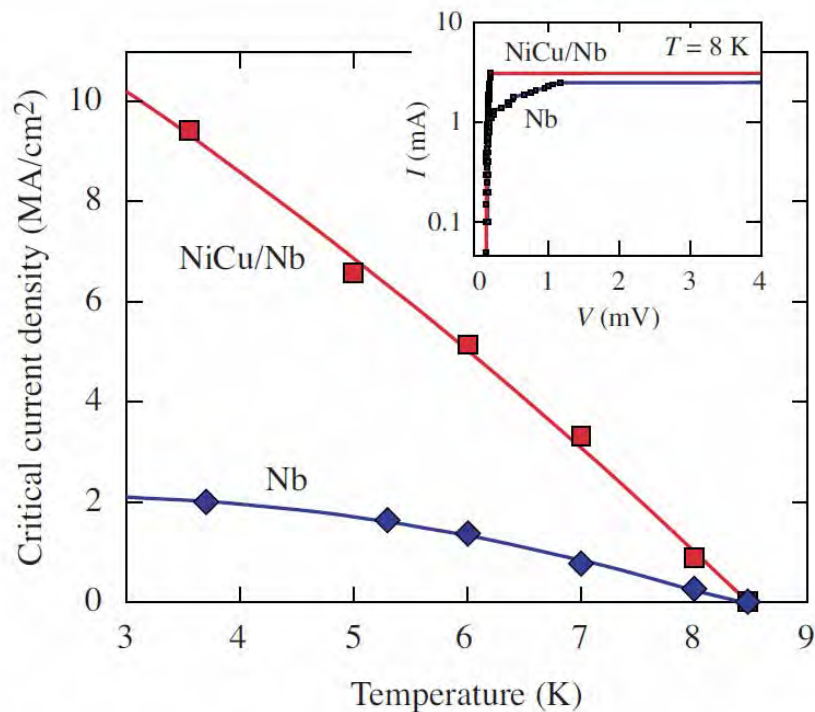


Figure 3.3 Critical current density dependence on temperature for NiCu/Nb and Nb microbridges. The inset shows the actual I - V characteristics in the semilogarithmic scale of both samples taken at 8 K.

3.3 Femtosecond, all-optical time-resolved spectroscopy

The most utilized ultrafast optical technique is a time-resolved optical pump-probe spectroscopy, in which photoinduced changes in the optical reflectivity or transmissivity of a sample under test are measured in the visible or near-IR region of the electromagnetic spectrum. This technique uses laser pulses both for optical excitation and probing, simultaneously providing a timing gate for measurement events and acts as a precise clock to control the generation and measurement of events. The idea of using a pulse to capture a transient event originated with the advent of high-speed spark photography [6]. Toepler performed the first pump-probe experiment in 1867 using a 2 μ s spark to generate a sound wave which propagation was photographed by a second spark that was triggered with an electrical delay [7].

The first pump-probe experiment that employed a short (10 ps) laser pulse was the measurement of the transient reflectance response of a germanium sample [8]. Recently, time resolution has been vastly improved with the development of femtosecond laser systems. The femtosecond pump-probe spectroscopy has been the most frequent tool for investigating the ultrafast nonequilibrium carrier dynamics in various electronic and optoelectronic materials.

3.3.1 Principle of pump-probe transient reflectivity experiments

The principle of pump-probe experiments is schematically shown in Fig. 3.4. A train of femtosecond optical pulses (typical pulse width ~ 100 fs) is split into two beams. One is a high-intensity pump beam, which is used to excite the sample under test and induce a transient change of the sample property (e.g., its reflectivity or transmittance). The other is a low-intensity probe beam (typical ratio of the pump-to-probe power is 10:1), which is used to monitor the pump-induced change. The probe beam is optically delayed with respect to the pump beam, which is realized through a computer-controlled delay line.

When the delay line is at the position before (1) in Fig. 3.4, the probe beam experiences a shorter optical path and arrives earlier than the pump beam on the sample. Since at this moment the pump has not arrived yet, the probe beam does not detect any change of the sample, so its reflectivity R does not change too. When optical delay line is at the position (1), the pump and the probe beams experience an equal-length optical path and arrive on the sample at the same time (zero delay). The probe beam begins to experience the pump-induced change and this change is linearly revealed to the reflectivity or transmittance change of the probe beam. The reflection or transition is recorded by the photo detector. In the next cycle, a subsequent laser pulse arrives at the beam splitter. The split probe beam arrives at the delay line again. The delay line is moved to position (2) and the probe beam has a longer optical path and reaches the sample some time after the pump beam. Now the probe beam “sees” a given point of the pump-induced transient. By repeating this process and plotting the

reflectivity or transmittance change of the probe beam as a function of the time delay between the two beams, we can map out the time-resolved pump-induced reflectivity or transmittance change of the sample, which after normalization can be denoted as $\Delta R/R$. One thing we need to note that the pump-probe experiment is not a real-time measurement, so we need to assume that the transients induced by each pump pulse are identical. Also the laser pulse width may have limitation for the pump-probe experiment result if the transient change is very fast. In our experiment results, we can see the rise time of the ultrafast transient change (sub ps scale or even faster) of the reflection is limited by our 100 fs laser pulse width.

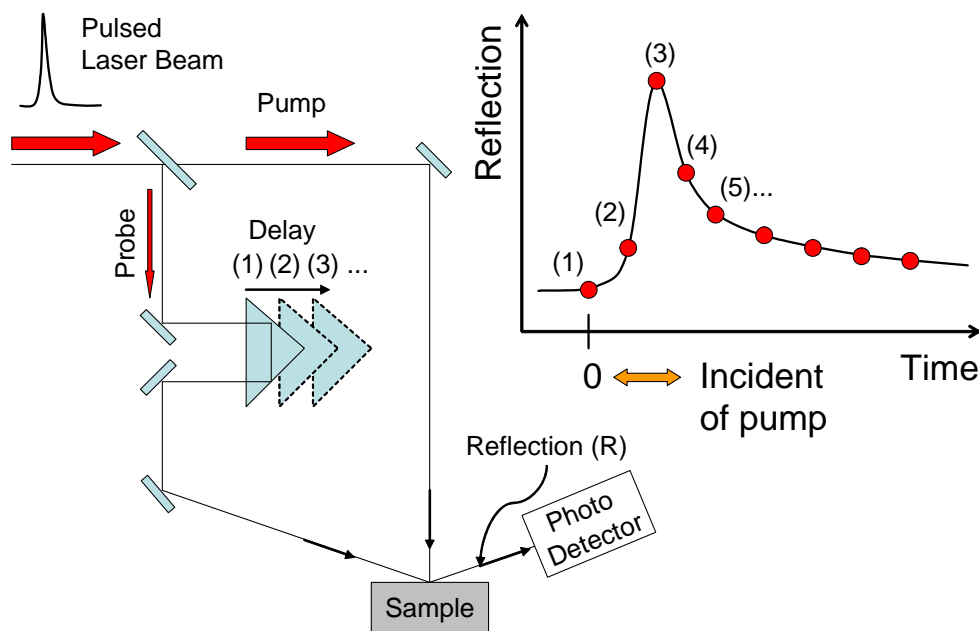


Figure 3.4 Principle of the pump-probe experiments.

3.3.2 Experimental setup

The experimental setup for the pump-probe measurements of F/S bilayers is shown in Fig. 3.5. We used a commercial Ti:Sapphire mode-locked laser (Coherent Mira A900F Laser), which produced a train of 100-fs-long pulses at the wavelength of 810 nm and the repetition rate of 76 MHz. The laser output was split into the pump and probe beams by a non-polarizing beam splitter. The light from the laser was linearly polarized and the polarization direction was horizontal. The pump beam passed through a half-wave plate to rotate the polarization from horizontal to vertical. Then, the amplitude (power) of the pump beam was modulated by the acousto-optic modulator (AOM) at the frequency of 200 kHz. The modulation signal was generated by the synthesizer and fed into the AOM. After that, the pump beam was focused onto the sample down to $<30 \mu\text{m}$ in diameter. As for the probe beam, it passed through the optical delay line controlled by a computer. Then, the probe beam went through a polarizer (horizontal) to make sure its direction of the polarization was orthogonally polarized to the pump beam. The probe beam was focused onto the test sample at similar diameter as the pump spot and its reflected signal was led to a horizontal analyzer. This horizontal analyzer was in front of a 125 MHz photodetector to prevent the reflected, vertically polarized pump beam from entering the detection system. The cross-polarized pump and probe arrangement was used to eliminate coherent artifacts caused by their direct interference that could arise around zero time delay [9]. The reflected probe-beam component was incident on the photodetector and converted to a voltage signal. After lock-in amplification of the

voltage signal, only the 200 kHz (modulated) frequency component was recorded by the computer.

In our experiments, typically the pump average incident power was maintained at ~ 5 mW and the pump/probe energy ratio was 10:1. Such conditions assured the absence of any trivial thermal effects, such as significant pump heating or probe influence, while assuring the good signal-to-noise ratio. It was possible to detect changes $\Delta R/R$ in of $\sim 10^{-6}$ in optimized experiments.

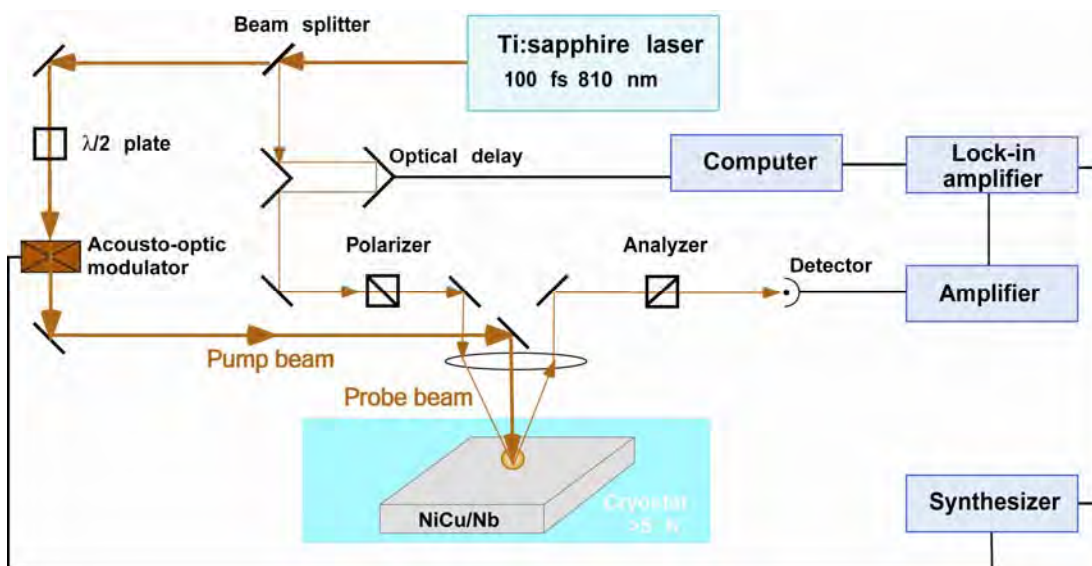


Figure 3.5 Pump-probe experimental setup for transient reflectivity measurement.

The F/S bilayer (sample under test) was placed in an evacuated optical, temperature-controlled cryostat and attached on a cold finger made of copper with adhesive glue (varnish), which had very good thermal conductivity at low temperatures. The cold finger was cooled down to 5 K by a continuous flow of liquid helium. The sample

temperature was controlled by a heater embedded in the cold finger and sensed by a temperature sensor (Si diode) attached on the cold finger next to the test sample. The temperature control precision of our system was ~ 0.1 K.

3.4 Time-resolved photoimpedance studies

Monitoring time evolution of voltage transients across a current-biased microbridge excited by optical pulses is another experimental method to study the photoresponse mechanism in superconducting materials. The time-resolved photoimpedance experiments mimic the photodetector operation. This technique has a direct applied implication in superconducting photodetectors.

Our test samples were "H"-type structures, patterned from 100-nm-thick Nb film and NiCu(21 nm)/Nb(70 nm) bilayers, and consisted of microbridges, placed between the signal line and the ground line of a 50- Ω coplanar stripline (CSL). The T_c of NiCu/Nb and pure Nb bridges were 8.5 K and 8.9 K, respectively, measured by the constant current method. The T_c decrease of NiCu/Nb can be explained by the proximity effect [10]. The actual T_c of the NiCu/Nb bilayer was estimated to be ~ 8 K from the temperature dependence of the Josephson critical current in tunnel junctions containing the same bilayer as an electrode [11]. The main specifications and microbridge dimensions are summarized in Table 3.1.

Table 3.2 $\text{Ni}_{0.48}\text{Cu}_{0.52}/\text{Nb}$ and pure Nb sample specifications.

	Sample A	Sample B
Thickness of Nb layer (nm)	100	70
Thickness of $\text{Ni}_{0.52}\text{Cu}_{0.48}$ layer (nm)	0	21
Width of the bridge (μm)	10	5
Length of the bridge (μm)	100	50

We used an experimental setup schematically shown in Fig. 3.6. The CSL with the microbridge was connected to the DC bias and RF output circuitry through a broadband, cryogenic bias-Tee and the whole arrangement was placed on a Cu cold-plate inside our temperature-controlled, continuous-flow helium cryostat. Outside the Dewar, the device output was fed to a low-noise broadband amplifier (bandwidth: 88 MHz to 9.3 GHz) characterized by a 44-dB gain. As a light source, we used in this case is a mode-locked IMRA fiber laser, generating 130-fs-wide pulses at the wavelength of 780 nm and the repetition rate of 50 MHz. The intensity of the incident radiation was attenuated in a very broad range using banks of neutral density filters. During the experiments, our samples were uniformly illuminated with the fluence per pulse in the $0.7 \text{ fJ}/\mu\text{m}^2$ to $10 \text{ fJ}/\mu\text{m}^2$ range at the bridge plane.

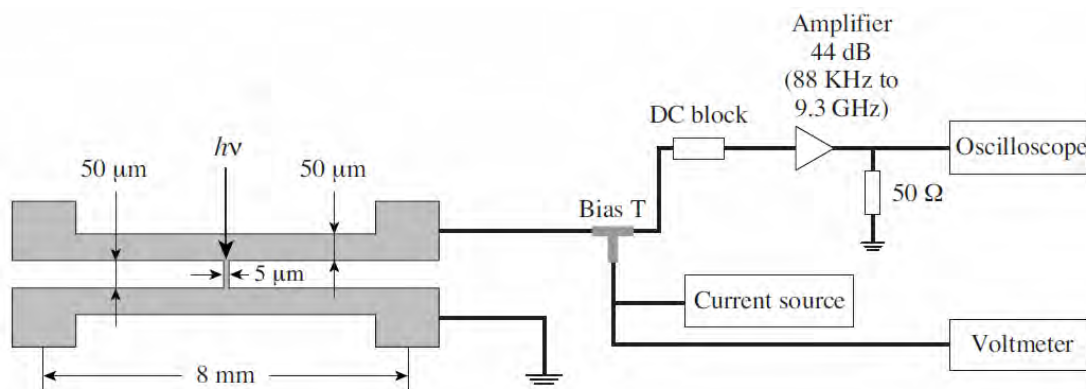


Figure 3.6 Time-resolved photoimpedance experiment setup.

References:

-
- ¹ G. P. Pepe, D. Pan, V. Pagliarulo, L. Parlato, N. Marrocco, C. De Lisio, G. Peluso, A. Barone, U. Scotti di Uccio, A. Casaburi, F. Tafuri, M. Khafizov, T. Taneda, and R. Sobolewski. Ultrafast Photoresponse of Superconductor/Ferromagnet Nano-Layered Hybrids. *IEEE Trans. Appl. Supercon.* 19, 376 (2009).
- ² T. Taneda, G.P. Pepe, L.Parlato, A.A. Golubov, and R. Sobolewski. Time-resolved carrier dynamics and electron-phonon coupling strength in proximized weak ferromagnet-superconductor nanobilayers. *Phys. Rev. B*, 15, 174507 (2007).
- ³ A. A. Golubov, M. Yu. Kupriyanov, and E. Il'ichev. The current-phase relation in Josephson junctions. *Rev. Mod. Phys.* 76, 411–469 (2004).
- ⁴ A. Angrisani Armenio, C. Cirillo, G. Iannone, S. L. Prischepa, and C. Attansio. Upper critical fields and interface transparency in superconductor/ferromagnet bilayers. *Phys. Rev. B*, 76, 024515 (2007).
- ⁵ A. Garcia-Santiago, F. Sánchez, M. Varela, and J. Tejada. Enhanced pinning in a magnetic-superconducting bilayer. *Appl. Phys. Lett.* 77, 2900 (2000); X. X. Zhang, G. H. Wen, R. K. Zheng, G. C. Xiong, and G. J. Lian. Enhanced flux pinning in a high-TC superconducting film by a ferromagnetic buffer layer. *Europhys. Lett.* 56, 119 (2001); J. M. E. Geers, M. B. S. Hesselberth, J. Aarts, and A. A. Golubov. Depairing currents in the superconductor/ferromagnet proximity system Nb/Fe. *Phys. Rev. B*, 64, 094506 (2001).

-
- ⁶ P. M. Norris, A. P. Caffrey, R. J. Stevens, J. M. Klopff, J. T. McLeskey, and A. N. Smith. Femtosecond pump-probe nondestructive examination of materials. *Rev. Sci. Instrum.* **74**, 400-406 (2003).
- ⁷ A. Toepler, *Ann. Phys. Chem.* **131**, 180 (1867).
- ⁸ D. H. Auston and C. V. Shank. Picosecond Ellipsometry of Transient Electron-Hole Plasmas in Germanium. *Phys. Rev. Lett.* **32**, 1120 (1974).
- ⁹ Z. Vardeny and J. Tauc. Picosecond coherence coupling in the pump and probe technique. *Optics Comm.*, 39(6):396 (1981).
- ¹⁰ A. I. Buzdin. Proximity effects in superconductor-ferromagnet heterostructures. *Reviews of Modern Physics*, 77, 935 (2005).
- ¹¹ G. P. Pepe, R. Latempa, L. Parlato, A. Ruotolo, G. Ausanio, G. Peluso, A. Barone, A. A. Golubov, Y. V. Fominov, and M. Y. Kupriyanov. Proximity effect in planar superconducting tunnel junctions containing Nb/NiCu superconductor/ferromagnet bilayers. *Phys. Rev. B*, 73, 054506 (2006).

Chapter Four: Time-resolved dynamics of carriers in NiCu/Nb nano-bilayers

In this chapter, I present my results on time-resolved optical pump-probe and photoimpedance studies of proximized F/S nanobilayers. The transient reflectivity measurement data have been fitted by the nonequilibrium 2-T and 3-T electron-heating models presented in Chap. 2. For the transient photoconductivity results, we used the kinetic inductive effect and the simple-resistive model.

4.1 Transient reflectivity experiment results

The time-resolved all-optical pump-probe method is a powerful technique to study the nonequilibrium carrier dynamics in metals, semiconductors, and superconductors. We can utilize this technique to extract parameters such as the position of the Fermi level, e - ph scattering time, phonon escape time, QP recombination time and/or excess QP numbers etc. In this thesis work, the femtosecond pump-probe has been implemented to study the photoresponse mechanism of superconducting F/S nanobilayers via transient reflectivity changes ΔR measurements, which is governed by the nonequilibrium QP dynamics.

The first time-resolved $\Delta R/R$ studies of F/S bilayers were performed in our group in 2007 and published by Taneda *et al.* [1]. Figure 4.1 shows the pump probe

results of pure Nb (70 nm) nano-layer sample, NiCu (6 nm)/Nb (70 nm), NiCu (21 nm)/Nb (70 nm) and pure Ni_{0.48}Cu_{0.52} (50 nm), respectively. It presents the dependence of the normalized reflectivity changes $\Delta R/R$ on the Ni_{0.48}Cu_{0.52} thickness at 6 K.

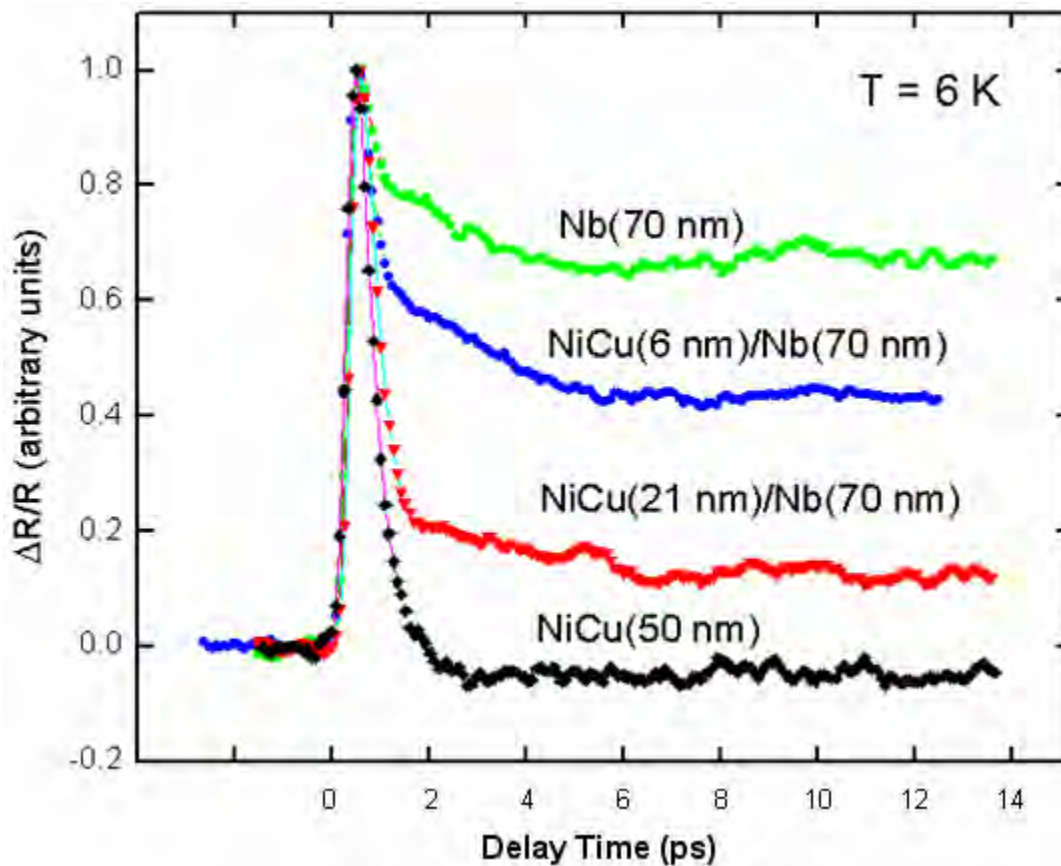


Figure 4.1 Normalized reflectivity change $\Delta R/R$ as a function of the time delay [1].

The waveforms shown in Fig. 4.1 are very representative for all our low-temperature measurements (including our own data). Within the experimental 10-ps-wide time window, the photoresponse signal for each sample showed an ultrafast rise, which is limited by the pump laser pulse width, and followed by biexponential decay

with the two characteristic time constants: τ_{fast} and τ_{slow} . The first one is sub-picosecond in duration and was identified as the electron-Debye (optical) phonon relaxation time, and its temperature dependence was later used by us to evaluate the $e-ph$ coupling constant g_{e-ph} in the proximized F/S heterostructures by calculating the density of state (DoS) functions for the tested bilayers. The slower relaxation time constant τ_{slow} (the order of a few picoseconds) was directly linked to the near band gap interaction of QPs with acoustic phonons.

Finally, after the initial relaxation, one can observe a $\Delta R/R$ plateau decayed with a hundreds of ps time scale, which is related to the bolometric phonon escape process. Comparing with the four waveforms, we can clearly see that the plateau level very strongly depends on the thickness of the NiCu overlayer. The pure Nb signal is dominated by the highest plateau level, and the plateau part is completely missing in the pure NiCu sample's signal. The above behavior shows that the phonon escape mechanism is dominated by the ultrafast anharmonic phonon decay in pure NiCu films and in the pure Nb case, the phonon escape more likely to be conducted through the Nb-substrate interface. Consequently, in the studied F/S bilayers, the optical response is weighted by the ratio of the thicknesses of the NiCu and Nb layers within the optical penetration depth. Obviously, the strongly suppressed bolometric plateau in F/S bilayers makes them as very attractive candidates for fast optical superconducting detectors application [1].

I have used the data from Taneda's time-resolved $\Delta R/R$ experiment, which were fitted only with the simplest two-exponential numerical method in his studies, and analyzed them with both the 2-T and 3-T models.

4.1.1 Two-temperature model fitting of NiCu/Nb and Nb samples

From the 2-T model point of view, the $\Delta R/R$ relaxation following τ_{slow} (essentially the plateau part within our time window) corresponds to the $T_{ph}(t)$ dynamics. It very strongly depends on the thickness of the NiCu overlayer, and the film/substrate acoustic transparency, which was denoted as τ_{es} in 2-T model, refer to Eq. (2.19) and Eq. (2.20).

Here, we are primarily interested in the $T_e(t)$ time evolution after the photon absorption, which is needed to estimate $L_{kin}(t)$ [Eq. (2.28)] and, eventually, predict the temporal shape of photoimpedance signals [Eq. (2.29)] measured in a setup presented in Fig. 3.7. Thus, we decided to focus on the $e-ph$ relaxation process and numerically solved the 2-T model [Eq. (2.19) and Eq. (2.20)], based on the energy balance relation $C_{ph}\tau_{e-ph} = C_e\tau_{ph-ph}$ under low-excitation fluencies and near T_c condition [2]. The resulting $T_e(t)$ and $T_{ph}(t)$ time evolutions are shown as solid lines, red and blue, respectively, in Fig. 4.2(a) and 4.2(b). We note that for both Nb and NiCu/Nb, the $T_e(t)$ and $T_{ph}(t)$ evolutions derived from the 2-T model solution fit the $\Delta R/R$ signal well. Especially in the case of the NiCu/Nb sample [Fig. 4.2(a)], the single-exponential $T_e(t)$ transient, represented by the τ_{e-ph} decay, fits the pump probe signal very satisfactorily. It emphasized that under the conditions of the pump-probe

experiment, $\Delta R/R$ is directly related to the T_e dynamics, which is governed by the nonequilibrium $e-ph$ relaxation [3].

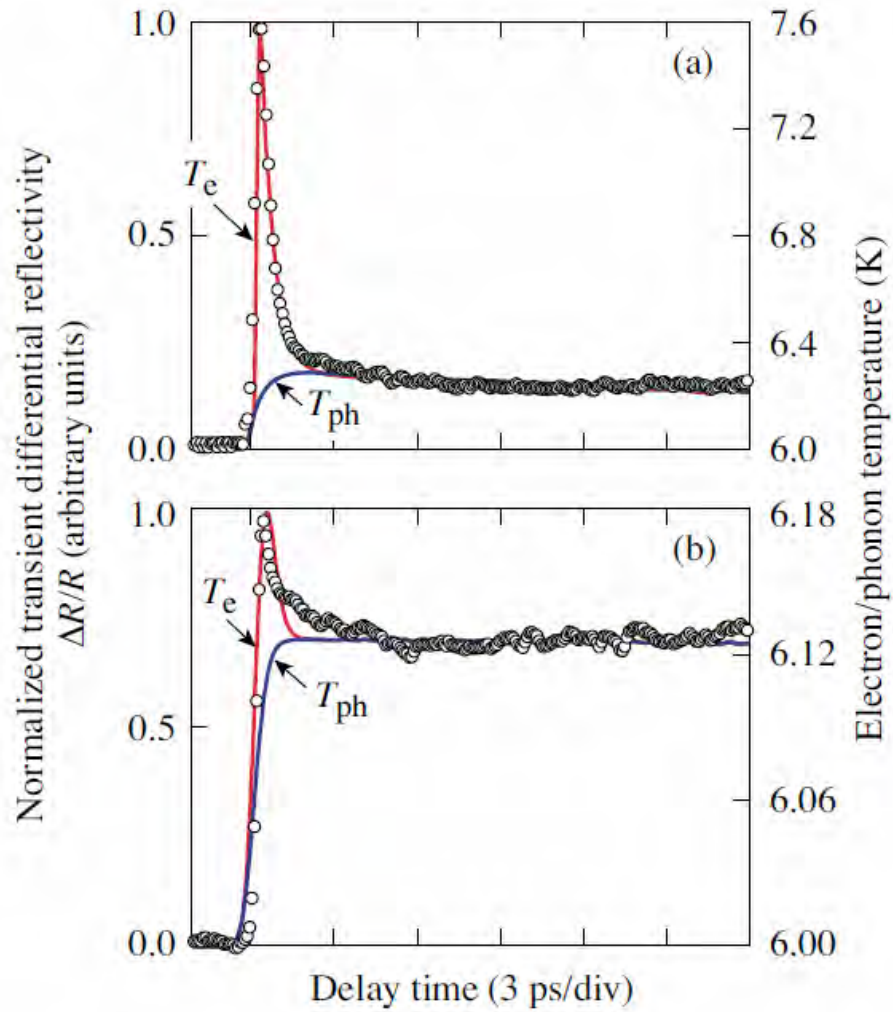


Figure 4.2 Normalized reflectivity change as a function of time (open circles), measured at 6 K for (a) NiCu/Nb and (b) Nb samples. The solid lines are the electron and phonon temperature transients, respectively, numerically evaluated for our films using the 2-T model [see Eq. (2.19) and Eq. (2.20)]. The right y axes show the actual increase in the electron/phonon temperature [3].

In our calculations, we assumed that the QPs are characterized by the Fermi distribution function, as our 100-fs pump pulse width is much longer than a few fs-long $e-e$ relaxation time. We also took into account that our 30- μm -diameter laser

beam spot size was much greater than the material optical penetration depth α , typically below 50 nm at the visible-light wavelength range, as well as the electron penetration depth (tens of hundreds of nm), so the one-dimensional model accurately represented our experimental situation. Finally, we neglected the heat diffusion out of the optical excitation region, since our experimental window was much shorter than τ_{es} , and assumed a Gaussian profile of the incident laser pump pulse.

The best fits presented in Fig. 4.2 were obtained from solving Eq. (2.19) and Eq. (2.20) with the following parameters: $C_{ph}/C_e = 2.7$, and $C_{ph}/C_e = 6.4$, for Nb and NiCu/Nb at $T_b = 6$ K, respectively, and the τ_{e-ph} equal to 0.46 ps and 0.21 ps in the fits to the early T_e relaxation parts of $\Delta R/R$ for our NiCu/Nb and Nb samples, respectively. Extracting the accurate values of τ_{es} was a difficult task due the short experimental time window of the $\Delta R/R$ transients. Thus, we could only get rough estimates and, accordingly, $T_{ph}(t)$ fits in Fig. 4.2 were obtained with τ_{es} on the order of ~ 300 ps and approximately 10-20 ns for NiCu/Nb and Nb, respectively. The maximum ΔT_e changes that were reached in NiCu/Nb and Nb samples during the laser pumping were 1.6 K and 0.18 K, respectively. On the other hand, the peak amplitude of the $T_{ph}(t)$ evolution for both samples was almost negligibly small since their ΔT_{ph} 's remained in the 2%–3% range of the bath temperature.

Comparing our τ_{e-ph} values, 0.46 ps for NiCu/Nb sample and 0.21 ps for Nb sample, with previous Taneda *et al.*'s experimental parameters [1], we found they are pretty close. Thus, we used them together with the previous experimental C_{ph}/C_e fit ratios and the g_{e-ph} values and the balance equation $C_{ph}\tau_{e-ph} = C_e\tau_{ph-e}$ in order to

calculate the actual values of C_e , C_{ph} , and τ_{ph-e} for our samples. The resulting values of C_e , C_{ph} , and τ_{ph-e} are 1.54 mJ/ (K cm³), 9.86 mJ/ (K cm³), and 2.9 ps for NiCu/Nb and 3.48 mJ/ (K cm³), 9.4 mJ/ (K cm³), and 0.57 ps for Nb, respectively. We note that both sets of specific heat values are different than those that Taneda *et al.* got before [1]. However, we must stress that previously the C_e values was deduced from DoS calculations which was numerically evaluated at the free surface of the top F layer without taking into account the actual spatial dependence of the DoS inside the two films and close to the interface. While the estimation of the C_{ph} for NiCu/Nb was based on the $C_{ph} = \beta_3 T^3$ law, where the coefficient β_3 in the bilayer was obtained by averaging the β_3 (Nb) and β_3 (NiCu) values with the layer thicknesses normalized to the optical penetration depth as weights [4]. The β_3 coefficient of the lattice heat capacity $\beta_3 = 25 \text{ J/K}^4\text{m}^3$ and $\beta_3 = 5 \text{ J/K}^4\text{m}^3$, again at $T_b = 6 \text{ K}$, for Nb and NiCu/Nb, respectively. Our presented set here of parameters is not only based on the experimental data but also much more realistic since in the case of NiCu/Nb the condition $C_{ph}/C_e \gg 1$ must be fulfilled in order to observe the transient photoresponse dominated by the electronic subsystem ($\tau_{e-ph}/\tau_{ph-e} \ll 1$) with a low value of the phonon plateau. At the same time, g_{e-ph} depends only on the averaged specific heat capacity and is much less sensitive to the C_{ph}/C_e ratio [3].

Comparing the (C_e and T_e) and (C_{ph} and T_{ph}) sets for the NiCu/Nb and Nb samples, we observe that the presence of the NiCu film only marginally affects the phonon subsystem with the only exception of the much shorter estimated τ_{es} value. Such behavior is expected as the bulk of the NiCu/Nb sample consists of the Nb film.

Although in both cases we have the same Nb-glass interface, the F overlayer acts as parallel heat sink, providing efficient anharmonic decay for the acoustic phonons and significantly reducing τ_{es} . However, the “phonon sink” is not the only role of the NiCu film in NiCu/Nb bilayers; a significant decrease in C_e and approximately ten times increase in the T_e peak value demonstrate that the electron subsystem cooling $\tau_{e-ph}/\tau_{ph-e} \ll 1$ is the dominant mechanism in the QP nonequilibrium relaxation in NiCu/Nb bilayers. Nevertheless, it is important to stress that it is difficult to properly derive the DoS for the actual NiCu-Nb interface and the DoS calculation presented in previous Taneda *et al.*'s research results is an apparent oversimplification due to the large atomic segregation of Ni atoms observed within the F/S interface volume of our samples, as we showed in Fig. 3.2 [1].

4.1.2 Three-temperature model fitting of NiCu/Nb and Nb samples

Figure 4.3 shows the time-resolved $\Delta R/R$ waveform in a semi-log scale in order to very directly see that the decay is double exponential, as it was observed by Taneda *et al.* [1]. In the previous section, as well as in our published data analysis [3], we used, however, the simplified 2-T model for fitting the data, in order to get a clear physical insight. Indeed, as presented in 4.1.1., the 2-T model gave us a very satisfactory description of the dynamics of the nonequilibrium superconductor excited by femtosecond optical pulses, the actual time-evolution of the photoresponse should include explicitly the experimentally observed τ_{fast} and τ_{slow} components.

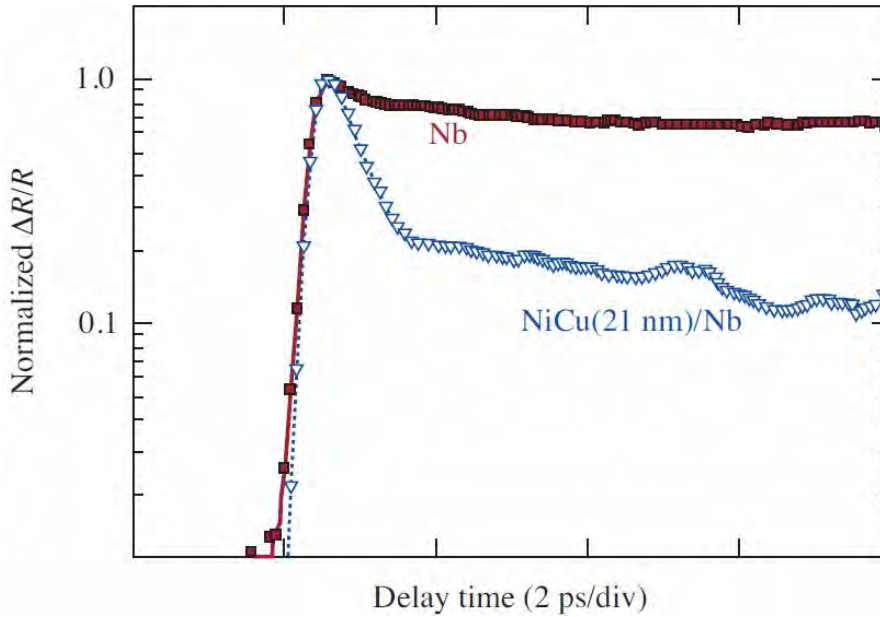
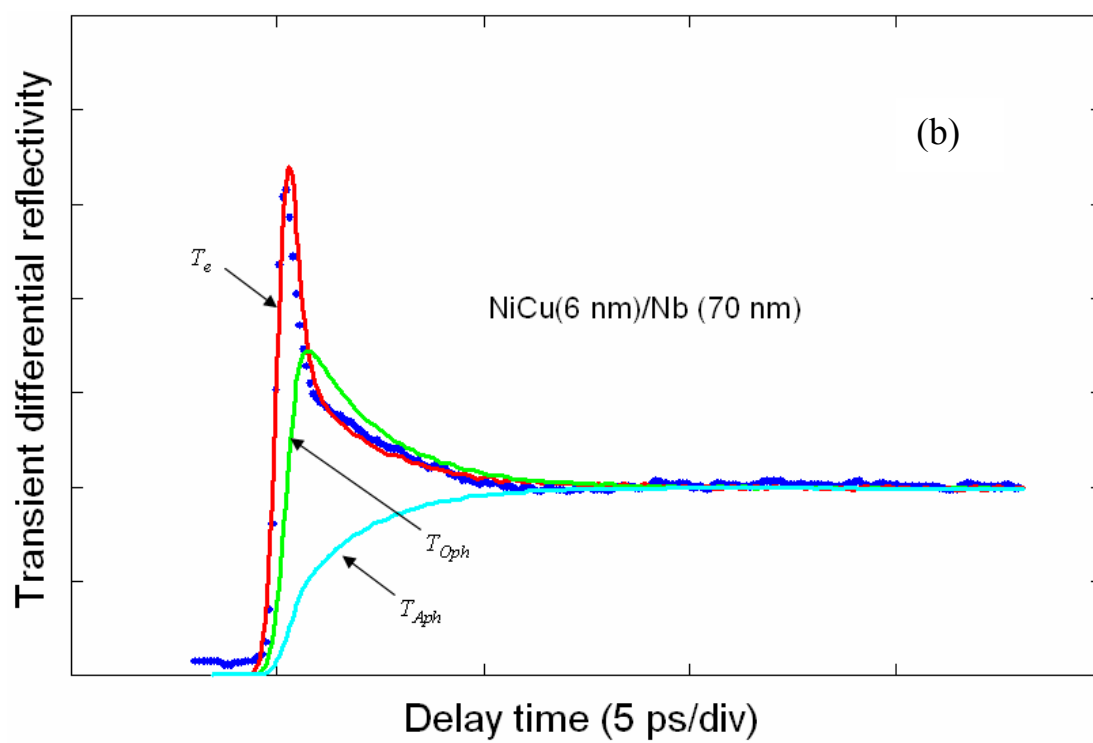
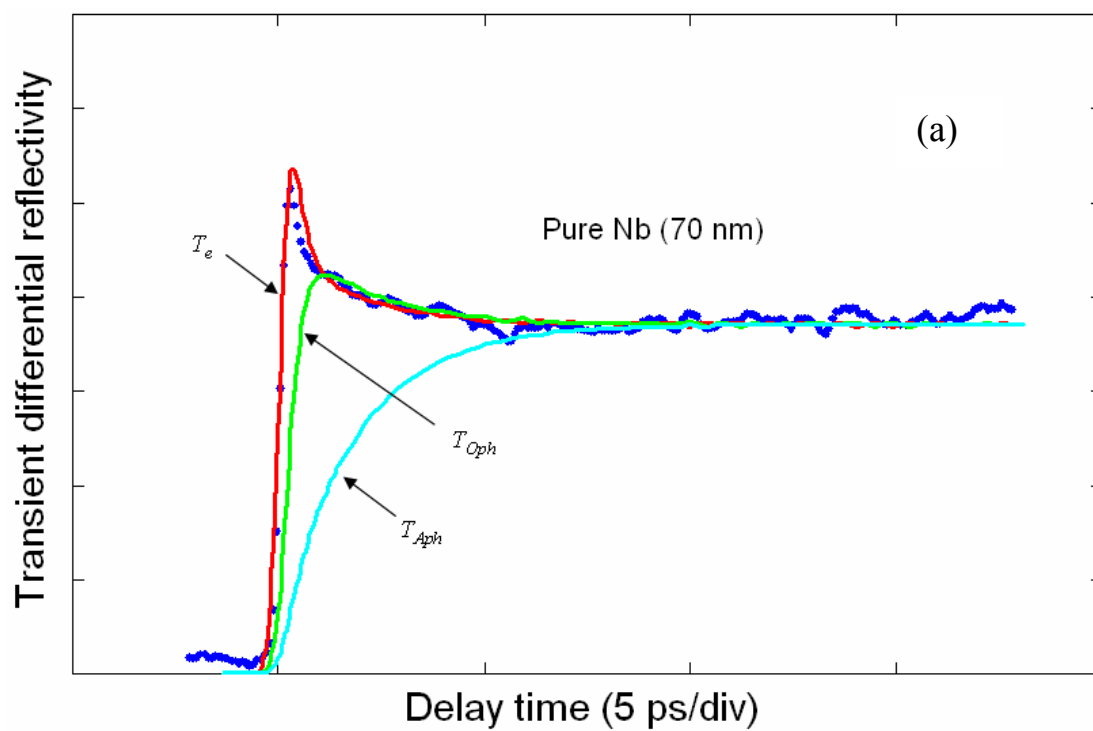
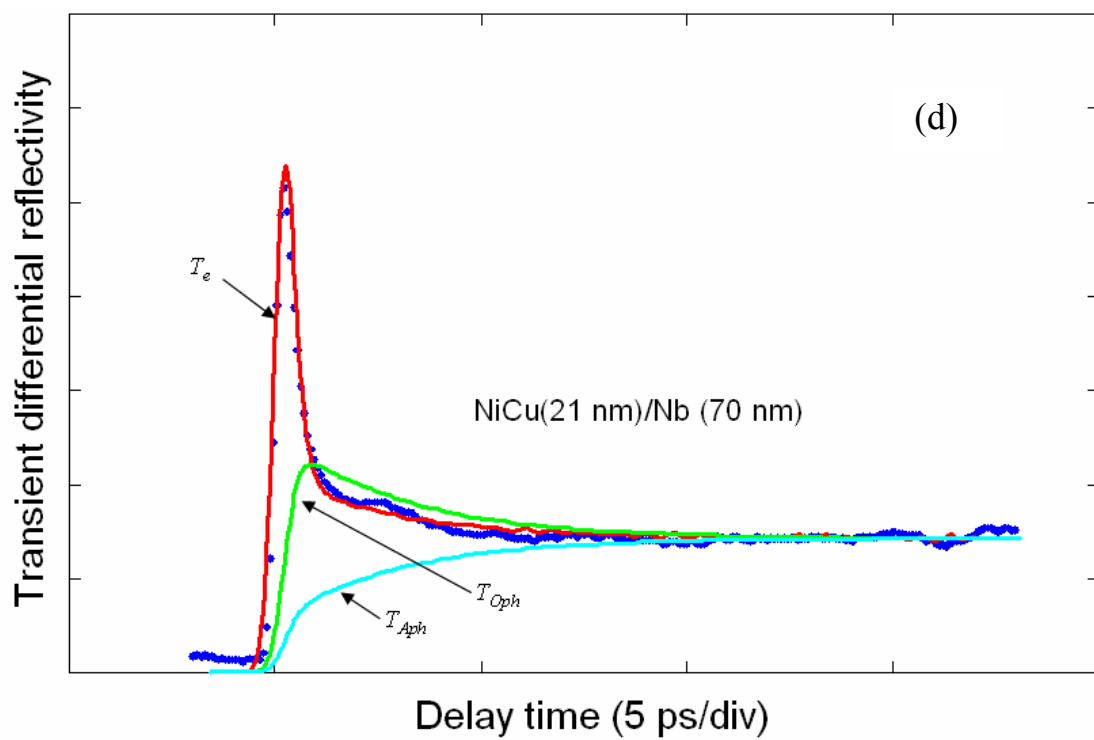
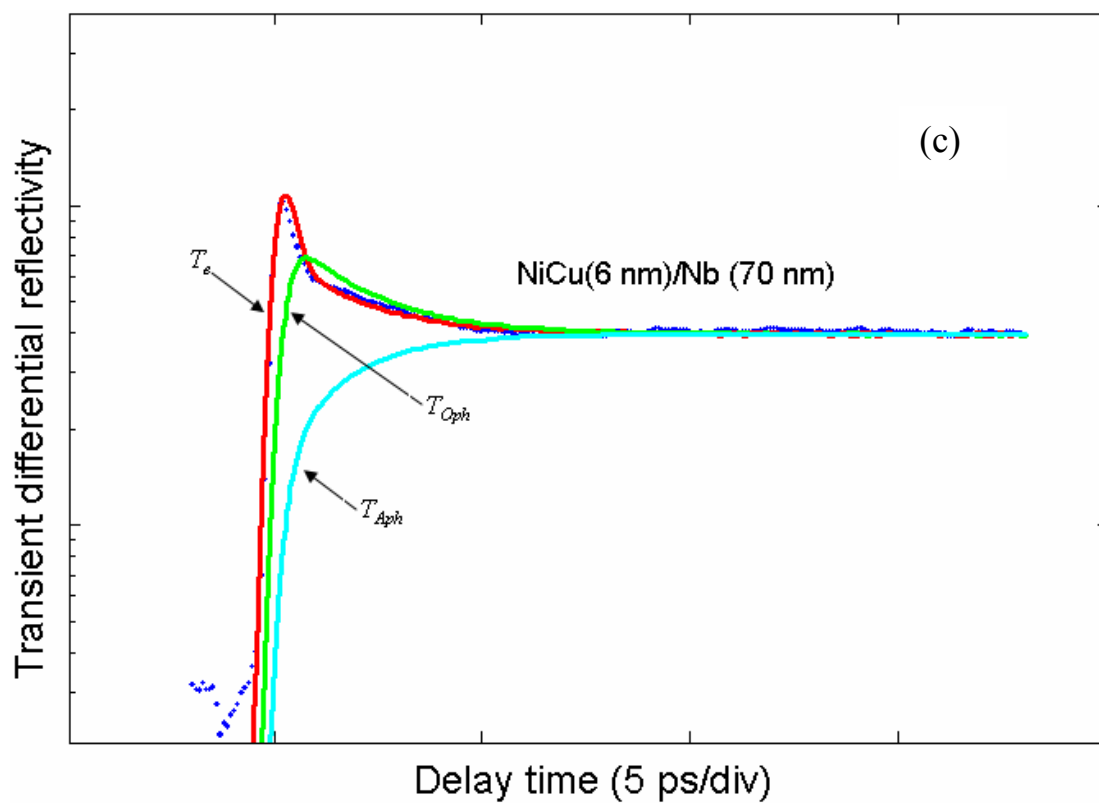


Figure 4.3 Time-resolved $\Delta R/R$ waveforms (semi-log scale) observed in a Nb(70 nm) thin film (red squares) and a NiCu (21 nm)/Nb (70 nm) bilayer (blue triangles) measured at $T = 6$ K

Thus, in the subsequent part of this Chap. we use our own 3-T model presented in Chap. 2 in order to separately evaluate the T_e , T_{Oph} and T_{Aph} transients numerically for our films pure Nb (70 nm), NiCu (6 nm)/Nb (70 nm), and NiCu (21 nm)/Nb (70 nm). Figure 4.4, summarizes our fitting results, obviously, the model curves fit experimental data more accurately than the ones generated by the 2-T model especially in the initial fast decay section. The latter is most clearly see in Figs. 4.4 (c) and (e), where the data is presented on a semi-log scale.

From the fitting results presented in Fig. 4.4, one can observe that the 3-T model models the double-exponential decay of the $\Delta R/R$ photoresponse transients. Comparing our τ_{e-Oph} and τ_{e-Aph} values from the 3-T model and the raw τ_{fast} and τ_{slow} decay times obtained by Taneda *et al.*'s [1], we can see that they are very consistent, as it is illustrated in Table 4.1.





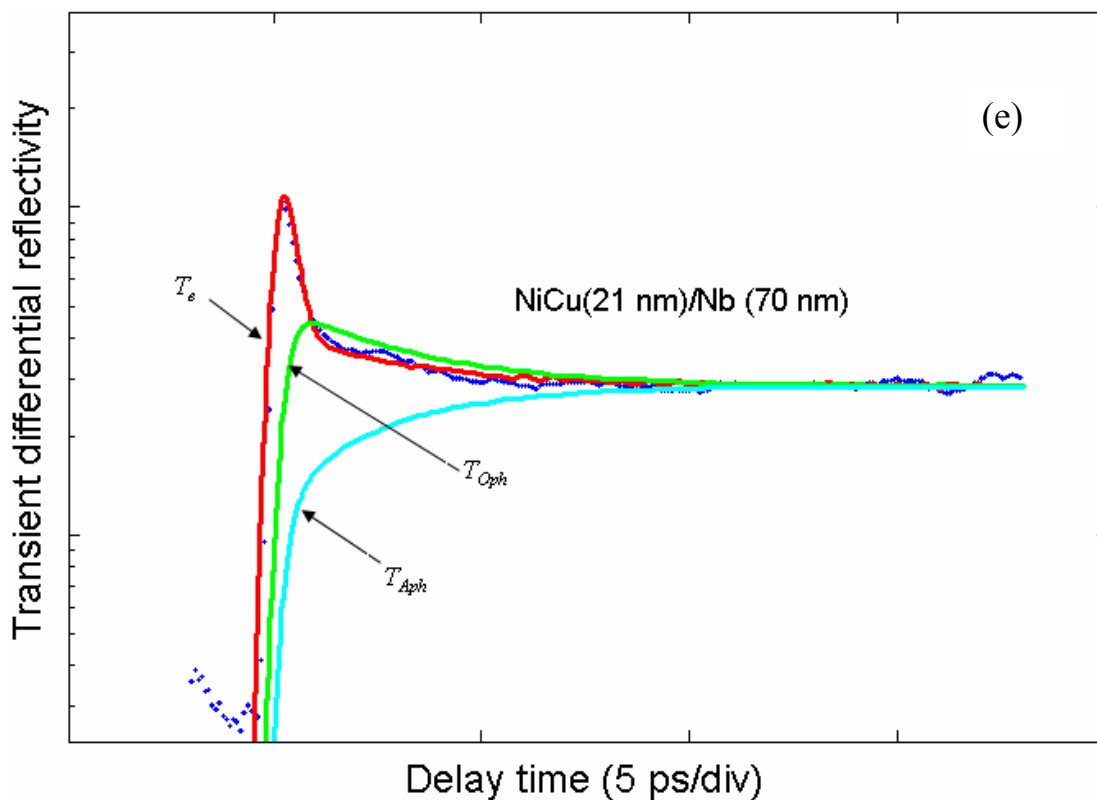


Figure 4.4 Numerical evaluation of the electron, optical phonon, acoustical phonon temperature transients for (a) pure Nb (70 nm), (b) NiCu (6 nm)/Nb (70 nm), (c) the same data as in (b) but in the semi-log scale, (d) NiCu (21 nm)/Nb (70 nm) and (e) the same data as in (d) but in the semi-log scale using the 3-T model [see Eq. (2.26) to Eq. (2.28)].

Table 4.1 The τ_{e-Oph} and τ_{e-Aph} fitting values from the 3-T model compared to the τ_{fast} and τ_{slow} components in Taneda *et al.*'s [1] two-exponential numerical method.

Samples	τ_{e-Oph} (ps)	τ_{e-Aph} (ps)	τ_{fast} (ps)	τ_{slow} (ps)
pure Nb (70 nm)	0.16	2.6	0.18	2.5
NiCu (6 nm)/Nb (70 nm)	0.29	3.9	0.27	4.1
NiCu (21 nm)/Nb (70 nm)	0.35	5.5	0.32	5.2

4.2 Transient photoimpedance experiment results

The sharp peak in the $T_e(t)$ dependence for NiCu (21 nm)/Nb (70 nm) in all our pump-probe data indicates that in the NiCu/Nb bilayers, the electron subsystem cooling is clearly the dominant mechanism in their nonequilibrium relaxation and, subsequently, according to Eq. (2.31), the microbridge made out of such bilayer should have a much stronger L_{kin} photoresponse compared to the one made out of pure Nb. The latter observation is directly supported by the $V_{kin}(t)$ photoimpedance transient simulations presented in Fig. 4.5.

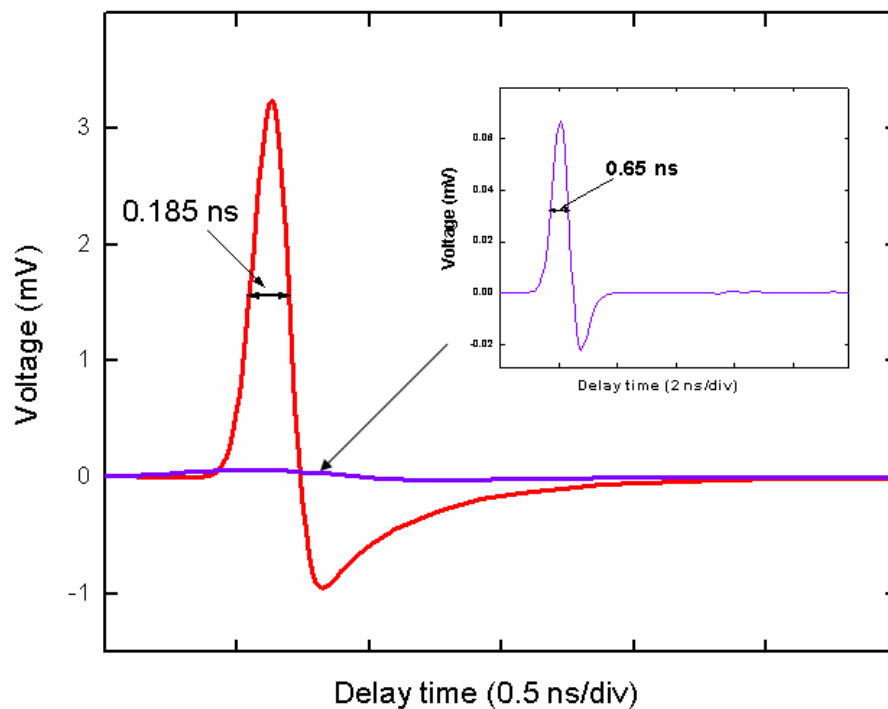


Figure 4.5 Numerical simulations of V_{kin} as a function of time, obtained using the 2-Tmodel solutions plotted in Figure 4.2 and Equations (2.31) and (2.32), for our NiCu/Nb (large oscillatory curve) and Nb (inset) samples. The bias current in both cases was $I_b/I_c = 0.43$.

The pronounced oscillatory transient with the FWHM of the main pulse equal to 185 fs corresponds to the NiCu/Nb microbridge, while essentially negligible, in the same voltage scale, response with FWHM = 650 fs (see inset in Figure 4.5) is that of the pure Nb bridge. In order to make this comparison meaningful, we assumed that the bridges had the same geometrical parameters and the ω_p values, and we inserted into Eq. (2.31) the digitized numerical dependences of $T_e(t)$ taken directly from our fits presented in Fig. 4.2. The bias current for both bridges [see Eq. (2.32)] was also taken to be the same and equal to $0.43I_c$.

4.2.1 Kinetic-inductive photoresponse transients of NiCu/Nb microbridge

Our experimental tests which were performed using the setup shown in Fig. 3.7 and on the sample types of the geometry listed in Table 3.1. They confirmed the predictions that based on Fig. 4.5, namely, we were unable to measure any kinetic-inductive signal in the case of a pure Nb bridge. On the other hand, the NiCu/Nb-bridge transient, while relatively weak, could be clearly resolved and is shown in Fig. 4.6. The waveform was measured at $T_b = 6.0$ K for a NiCu (21 nm)/Nb (70 nm) microbridge, illuminated with 100-fs optical pulses of ~ 7 μ W of the incident average power, and biased with $I_b/I_c = 0.43$. Despite a relatively large level of the noise of the presented transient, its oscillatory nature (positive main pulse, followed by a negative component), which is typical for the superconductive L_{kin} response shown in Fig. 4.5,

can be clearly observed. The thermal contribution was negligible, as under our experimental conditions. The increase of T_{ph} was negligible for NiCu (21 nm)/Nb (70 nm) and we could easily fit the experimental waveform by the simple $V_{\text{kin}}(t)$ expression [Eq. (2.32)-solid line in Fig. 4.6] obtained in the same way as the NiCu/Nb transient shown in Fig. 4.5, with the only exception that the fit had to be numerically stretched by including a high-bandpass filter, corresponding to the upper limit (9.3 GHz) of the bandwidth of our amplifier, in order to concur with the experimental main pulse FWHM = 690 ps, limited by our front-end electronics.

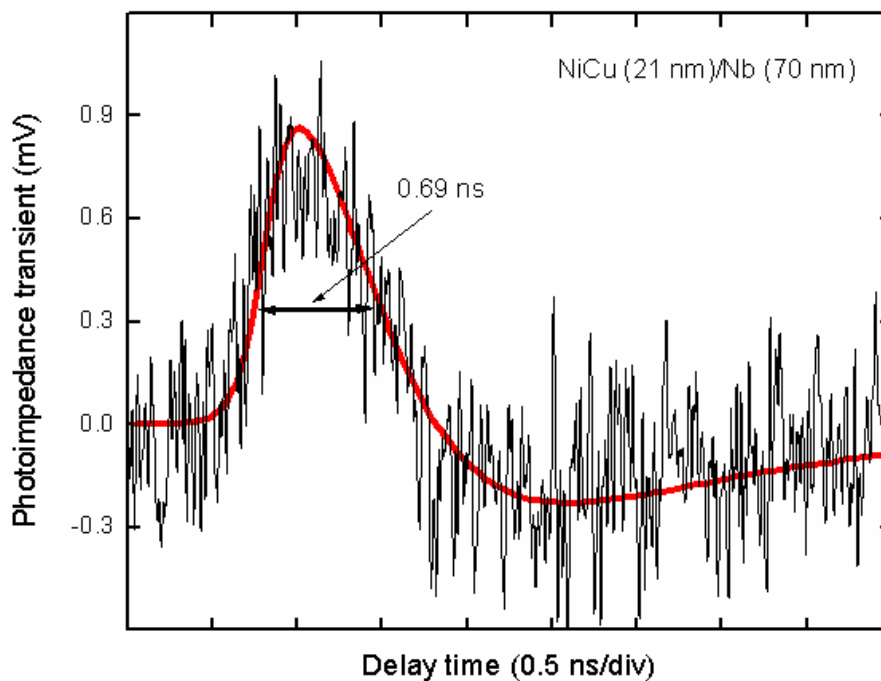


Figure 4.6 Experimental photoresponse transient of a NiCu/Nb microbridge, acquired at 6 K with $I_b = 4.5$ mA ($I_b/I_c = 0.43$). The solid (red) line is the fit based on the kinetic-inductive model (see Figure 4.5), numerically stretched in order to account for the limited bandwidth of our output amplifier.

The $V_{\text{kin}}(t)$ fit in Fig. 4.6 allowed us to estimate the maximum L_{kin} value of ~ 50 nH for our NiCu/Nb microbridge. In a proximized bilayer, the relation between L_{kin} and the superconductivity magnetic penetration depth λ is not obvious, since any estimation needs to take into account the spatial dependence of the superconducting order parameter. Nevertheless, if we roughly assume that $L_{\text{kin}} \approx (\mu_0 \lambda^2 I)/(wd)$, we get $\lambda \approx 1$ μm at the reduced temperature of our experiment. The obtained λ is much larger than 100 nm typically quoted for pure Nb, but considering the weak ferromagnetic nature of the NiCu overlayer, we find it to be quite reasonable [5].

4.2.2 Bolometric photoresponse transients of Nb microbridge

In the case of our pure Nb bridges, we could only obtain a photoresponse signal by significantly increasing the incident optical power or/and maintaining the sample at temperature very close to T_c . Fig. 4.7 presents a photoresponse waveform measured for our Nb sample biased with $I_b/I_c = 0.43$, the same as in the case of the NiCu (21 nm)/Nb (70 nm) sample in Fig. 4.6, but illuminated with 225 μW of optical power and maintained at 7 K. The over 30 times increase of the optical excitation resulted a large and relatively slow (FWHM ~ 10 ns) transient, which, in this case, could be interpreted as simple (Joule-type) optical heating. The incident photons not only broke all the Cooper pairs in the superconductor, but also substantially heated up the entire bridge, leading to a temporary increase of the sample temperature above T_c .

The solid line in Fig. 4.7 was obtained by using the resistive voltage response formula, Eq. 2.30. As we stated in Chap. 2, $\Delta T(t)$ in Eq. 2.30 is in this case

the increase in T_{ph} of our system obtained from Eq. (2.19) and Eq. (2.20) [see Fig. 4.2(b)]. With τ_{es} fitted to the transient photoresponse dependence presented in Fig. 4.7, we note that $\tau_{es} \approx 18$ ns, in very good agreement with our earlier predictions based on Eq. (2.25).

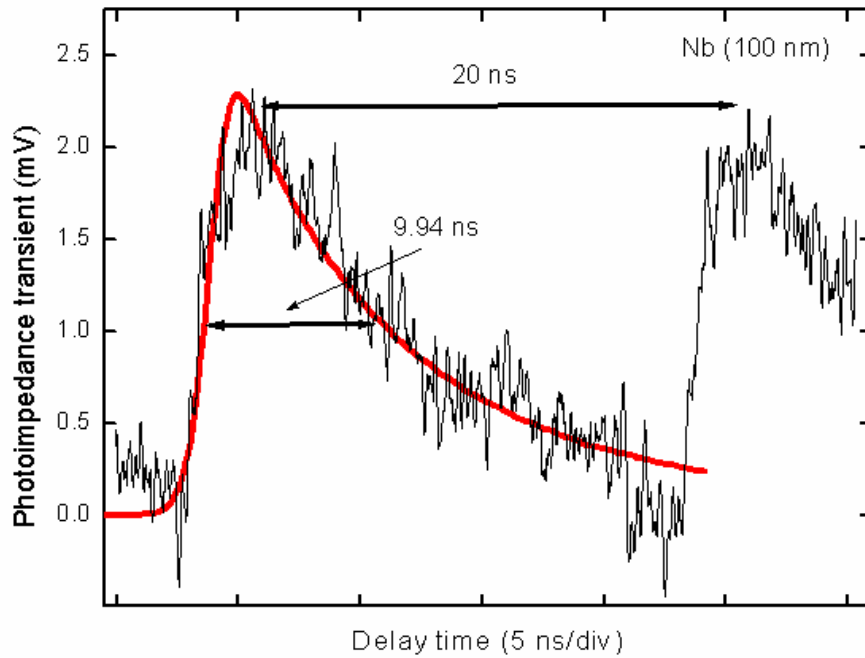


Figure 4.7 Experimental photoresponse transient of a pure Nb microbridge, acquired at 7 K with $I_b/I_c = 0.43$. The solid (red) line is the fit based on the simple-resistive model [see Eq. (2.30)]. The incident optical pulse repetition time was 20 ns.

4.3 Summary

In Chapter 4, we presented femtosecond time-resolved optical pump-probe and photoimpedance studies and data analysis of proximized F/S hybrids nanobilayers consisting of $\text{Ni}_{0.48}\text{Cu}_{0.52}$ layers deposited on top of Nb films. The weak ferromagnetic nature of the completely proximized $\text{Ni}_{0.48}\text{Cu}_{0.52}$ film makes possible to observe the dynamics of the nonequilibrium superconductivity through the near-surface optical reflectivity change measurements. A thin layer of NiCu strongly reduces the slow bolometric component of Nb films, producing an optical response of only few ps relaxation width.

The results presented by us in this thesis are promising in view of potential applications as ultrafast kinetic inductance superconducting photodetectors as confirmed by preliminary time-resolved photo-impedance experiments on Nb as well as NiCu (21nm)/Nb (70nm) samples. Both the optical pump-probe and photoimpedance results have been fitted by our models very well. We also showed that the 3-T model, the true two exponential decay fitting, is the most suitable for fitting the actual, experimental photoresponse signals of nonequilibrium superconducting thin films.

References:

-
- ¹ T. Taneda, G. P. Pepe, L. Parlato, A.A. Golubov, and R. Sobolewski. Time-resolved carrier dynamics and electron-phonon coupling strength in proximized weak ferromagnet-superconductor nanobilayers. *Phys. Rev. B* 15, 174507 (2007).
- ² A. D. Semenov, R. S. Nebosis, Yu. P. Gousev, M. A. Heusinger, and K. F. Renk. Analysis of the nonequilibrium photoresponse of superconducting films to pulsed radiation by use of a two-temperature model. *Phys. Rev. B*, 52, 581 (1995).
- ³ D. Pan, G. P. Pepe, V. Pagliarulo, C. De Lisio, L. Parlato, M. Khafizov, I. Komissarov, and Roman Sobolewski. Layered ferromagnet/superconductor heterostructures: nonequilibrium quasiparticle dynamics and photodetector applications. *Physical Review B*, 78, 174503 (2008).
- ⁴ Y. S. Touloukian and E. H. Buyco, Specific Heat: Metallic Elements and Alloys. *Thermophysical Properties of Matter*, 4 (IFI/Plenum, New York) (1970).
- ⁵ J. H. Claassen, S. Adrian, and R. J. Soulen, Jr.. Large Non-linear Kinetic Inductance in Superconductor/Normal Metal Bilayer Films. *IEEE Trans. Appl. Supercond.* 9, 4189 (1999).

Chapter Five: Transient reflectivity measurements of F/S hetero-structures formed by perovskite oxide materials

As we mentioned in Chap. 2, superconductors are usually classified into two groups: conventional or LTS, and HTS. LTS are most often metallic elements or compounds with $T_c < 40$ K, while HTS are associated with the perovskite copper-oxide-based (CuO_2) materials with T_c above 40 K. HTS applications have attracted enormous scientific and commercial attention ever since discovery of superconductivity in ceramic materials by J. Georg Bednorz and K. Alexander Müller [1] from IBM Zurich Research Laboratory, who shared the Nobel Prize in Physics 1987. The very high T_c of those materials opened promising prospects of devices and systems that required only liquid nitrogen cooling, rather than liquid helium cooling.

The BCS theory provides the basis for understanding superconductivity in conventional superconductors. On the contrary, the weak coupled e - ph interaction from the BCS theory is not sufficient to account for the high T_c values observed in cuprate HTS materials. The origin of this high T_c and the microscopic pairing mechanism in HTS materials still remain open. The crystal structures of HTS materials are more complex compared to the LTS.

Lacking in theory for HTS, several optical measurements were performed on $\text{YBa}_2\text{Cu}_3\text{O}_{7-\delta}$ (YBCO), the most studied of the HTS. Fig. 5.1 showed the crystalline structure of YBCO with its orthorhombic unit cell. It is widely accepted that superconductivity resides within the copper-oxide planes, i.e., the supercurrent mainly flows within the CuO_2 planes. The charge reservoir layers below and above CuO_2 planes can accept or donate electrons to the conducting CuO_2 slab. Charge carriers are added by doping, either by substituting different valence ions or by changing the oxygen concentration. As a consequence, the superconducting properties depend strongly on the doping level. It is known that the oxygen content can be varied, leading to the transition from an insulating (anti-ferromagnetic) material for $\delta > 0.7$ to a superconducting material with $T_c \approx 90$ K for $\delta = 0.05$ [2].

The energy gap in HTS materials is generally believed to be highly anisotropic and has a d-wave symmetry instead of s-wave, as in the LTS materials. The d-wave symmetry has nodal regions where the gap value is zero. Although there have been conflicting reports of the superconducting energy gap ranging from $2\Delta \approx 8k_B T_c$ [3,4], to $2\Delta \approx 3.5k_B T_c$ [5], the general consensus is that YBCO has an energy gap in the range of several tens of meV, more than one order of magnitude bigger than the gap values for LTS materials. The Δ values of HTS correspond to frequencies in the few THz range, or alternatively, in the far-infrared part of the radiation spectrum.

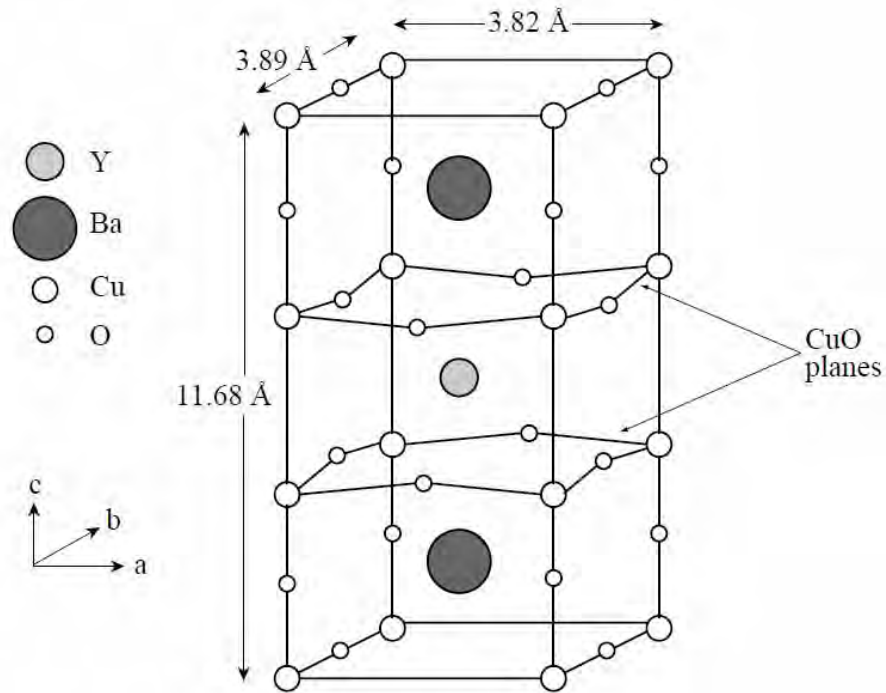


Figure 5.1 The unit cell of $\text{YBa}_2\text{Cu}_3\text{O}_{7-\delta}$ showing the location of the CuO_2 planes which are believed to contain the superconducting current.

The choice of material is crucial since various superconductors have a drastically different kinetic response in terms of the τ_{e-ph} scattering, C_e/C_{ph} ratio, and τ_{es} . Devices based on HTS compounds, such as YBCO, are particularly interesting since their λ_L is ~ 200 nm and their $e-ph$ relaxation time τ_{e-ph} is of the order of a few ps [6]. YBCO has already been demonstrated to be a rather optimal choice for bridge-type superconducting photodetectors, as YBCO microbridges are characterized by the overall picosecond photoresponse [7]. Thus, they should become the photon counters of choices, once we are able to reproducibly grow and pattern YBCO nanostructures.

Besides the aforementioned conventional, metallic proximity bilayers, much interest has been recently devoted to novel oxide multi-layer structures. Among them, we focus our attention on the YBCO/NiCu and YBCO/manganite bilayers. The latter heterostructures are especially interesting since manganites, i.e., LaSrMnO (LSMO), have unique physical properties related to their high spin polarization in the ferromagnetic state at $T < T_{Cu} \sim 300$ K. In the presence of a spatially inhomogeneous Δ , λ_L is not constant through the film thickness, and it is possible to write:

$$\frac{\mu_0}{L_{kin}} = \int \frac{dx}{\lambda_L^2(x)} , \quad (5.1)$$

where the integral is taken across the film thickness. Proximized bilayers show a spatial modification of Δ along the N layer [8], and this physical characteristics are going to affect the electronic response in the presence of a nonequilibrium state through the modification of the electron distribution function [9].

Similar to the femtosecond time-resolved optical pump-probe measurements that we performed on NiCu/Nb and pure Nb samples, we have also performed preliminary studies of the $\Delta R/R$ transients on different groups of NiCu/YBCO and LSMO/YBCO nano-bilayers both, whose preparations were listed in Chap. 3. Our experiments performed on YBCO-based samples confirmed that the F film also enhanced the QP dynamics in proximized HTS samples.

5.1 NiCu/Au/YBCO F/S nano-bilayers

For NiCu/Au/YBCO bilayer structure, the roughness of the YBCO film was estimated to be lower than 2 nm. Typical T_c of the pure YBCO was ~ 89 K and T_c of NiCu (21 nm)/Au/YBCO (100 nm) trilayer was ~ 81 K.

Figure 5.2 presents $\Delta R/R$ transients for both the plain YBCO and NiCu (20 nm)/Au (10 nm)/YBCO (100 nm) heterostructures. As in the LTS case, the relaxation process is bi-exponential. However, it is much less pronounced than that in the Nb and NiCu/Nb cases. The double-exponent fitting procedure applied to curves in Fig. 5.2 (solid line and dashed line) gave $\tau_{fast} = 1.32$ ps and $\tau_{slow} = 2.7$ ps, and $\tau_{fast} = 0.35$ ps and $\tau_{slow} = 2.8$ ps for the YBCO and NiCu/Au/YBCO samples, respectively. Presence of the F surface layer significantly speeded up the early phase of the relaxation dynamics (τ_{fast}), while the QP interaction with acoustic phonons (τ_{slow}) remained essentially the same. The latter indicates the phonon-escape process governed by the acoustic phonons is independent of the F film, as expected, since it occurs at the YBCO/substrate interface.

The above observation is additionally supported by the 3-T model fitting presented in Fig. 5.3 for the NiCu/Au/YBCO sample. Comparing the parameter values of $\tau_{e-Ph} = 0.42$ ps and $\tau_{e-Aph} = 3.1$ ps obtained from the 3-T model (Fig 5.3) with the τ_{fast} and τ_{slow} values in the two-exponential numerical method (Fig 5.2), we can see they are reasonably close to each other. At the same time, we note that the overall contribution of acoustic phonons (blue line) is almost negligible.

We want to stress again that so far there are no good theoretical models for the proximity effect in the HTS-based S/F systems. Thus, our measurements have an important basic-physics interest in the investigations of nonequilibrium effects in correlated systems. In view of potential photodetector applications, it is also important to mention that our metallic overlayer has a unique double-utility, as it also acts as a protective layer for YBCO during the fabrication processing (performed on oxide films bridge patterning), as well as during the subsequent experiments. Recently, YBCO microbridges with widths down to several hundreds of nanometers have been reported [10], making nanowire-type HTS devices a reachable goal.

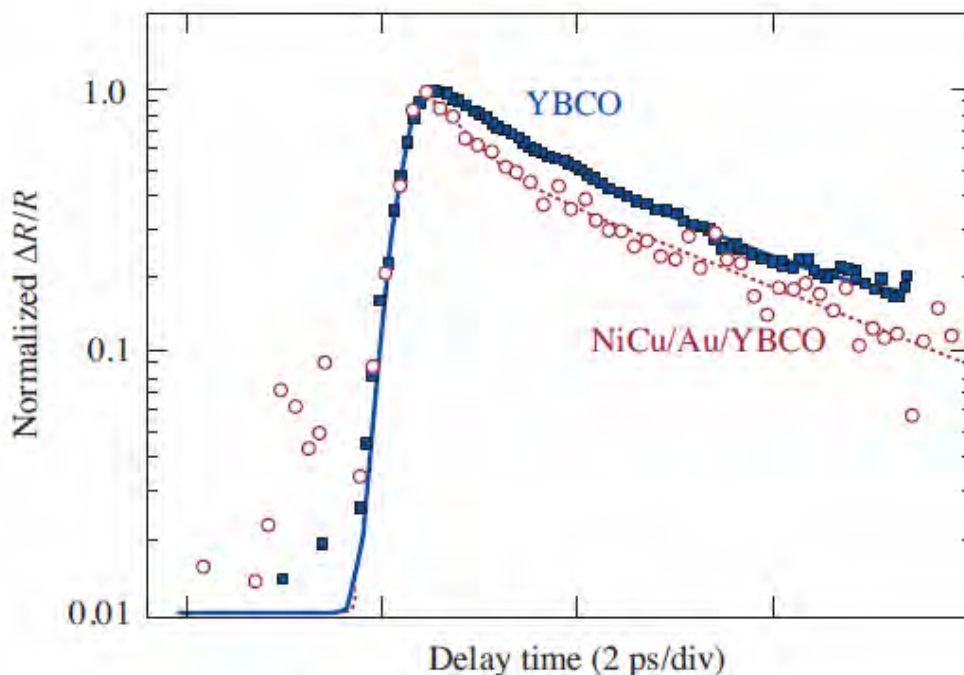


Figure 5.2 Time-resolved $\Delta R/R$ waveforms (semi-log scale) observed in a 100-nm YBCO thin film (black squares) and a NiCu (12 nm)/Au (10 nm)/YBCO (100 nm) bilayer (red open circles) measured at $T = 5$ K. The dashed lines are bi-exponential fits.

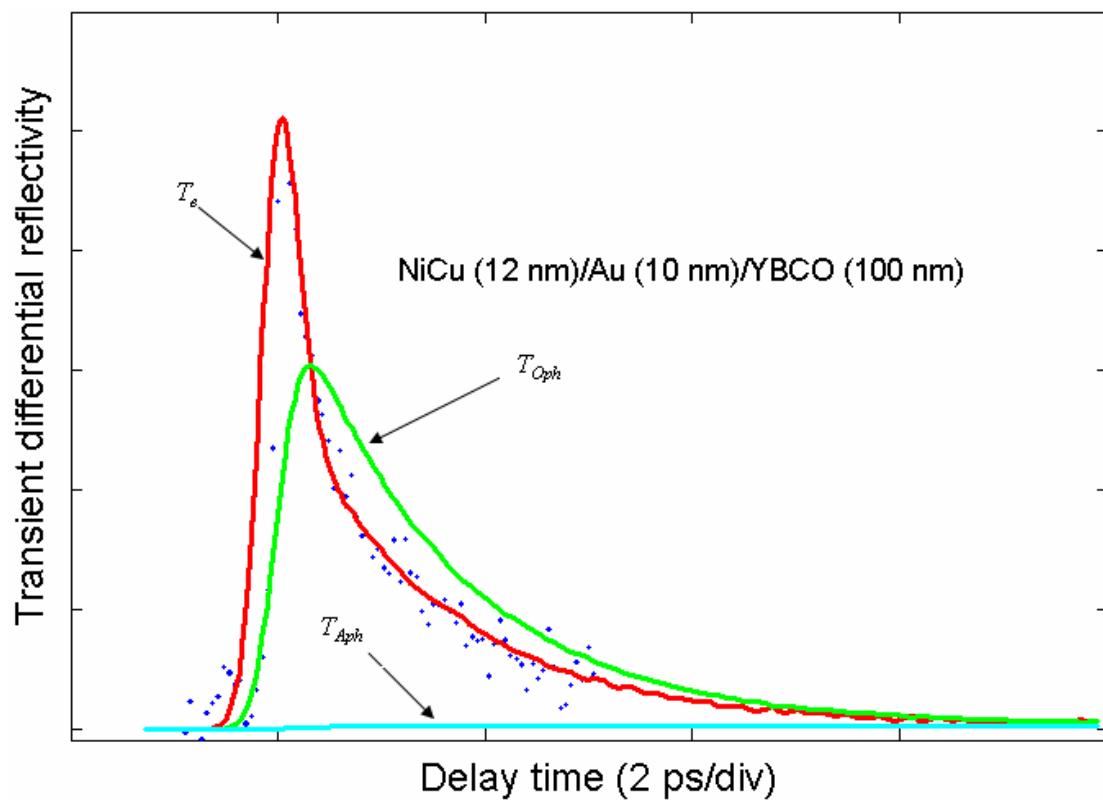


Figure 5.3 Numerical evaluation of the electron, optical phonon, acoustical phonon temperature transients for NiCu (12 nm)/Au (10 nm)/YBCO (100 nm) bilayer using the 3-T model [see Eq. (2.26) to Eq. (2.28)].

5.2 LSMO/YBCO F/S nano-bilayers

In the LSMO/YBCO bilayer structure fabrication process, our YBCO films exhibited excellent properties, in terms of both their structure and transport properties, with the sharp superconducting transition ($T_c = 91.5$ K, $\Delta T_c \sim 0.3$ K). From the LSMO plot of the conductivity versus temperature (see Fig. 3.4), we could deduce that T_{Cu} , defined as the crossover temperature between the paramagnetic (PM) and ferromagnetic (FM) states, exceeded room temperature, i.e., our LSMO film was in the FM state in the whole range of temperatures of our interest.

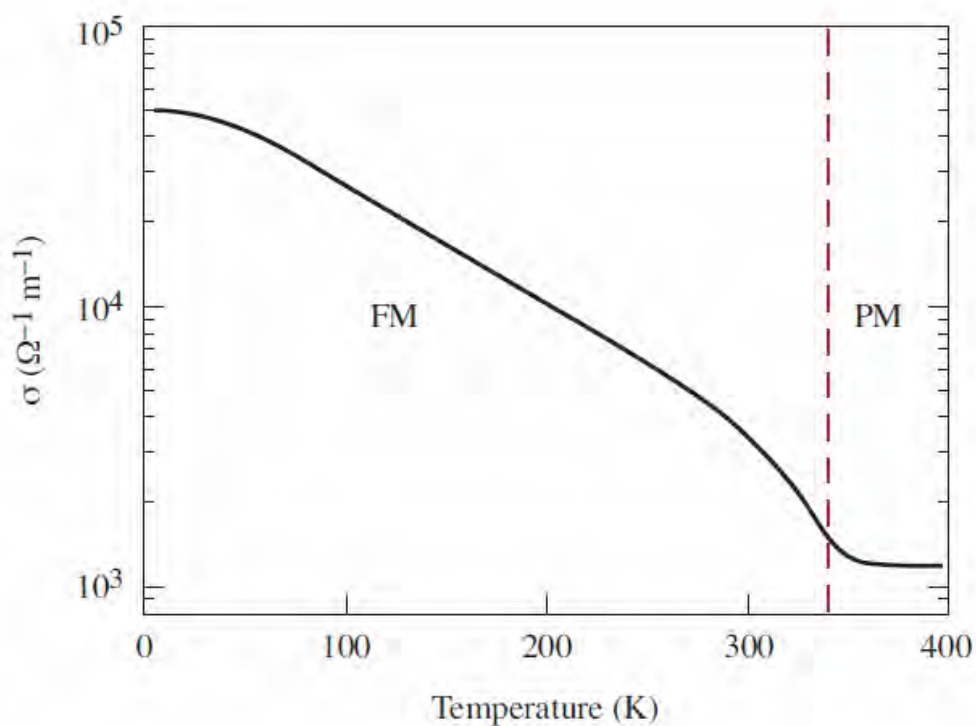


Figure 5.4 Direct-current (dc) conductivity versus temperature of a LSMO film.

Our experimental $\Delta R/R$ trace in the case of a LSMO/YBCO heterostructure is shown in Fig. 5.5 and again compared to the response of a pure YBCO film. We see that the dynamical reflectivity of the LSMO/YBCO bilayer demonstrates a very pronounced shortening of the relaxation time in recovering equilibrium.

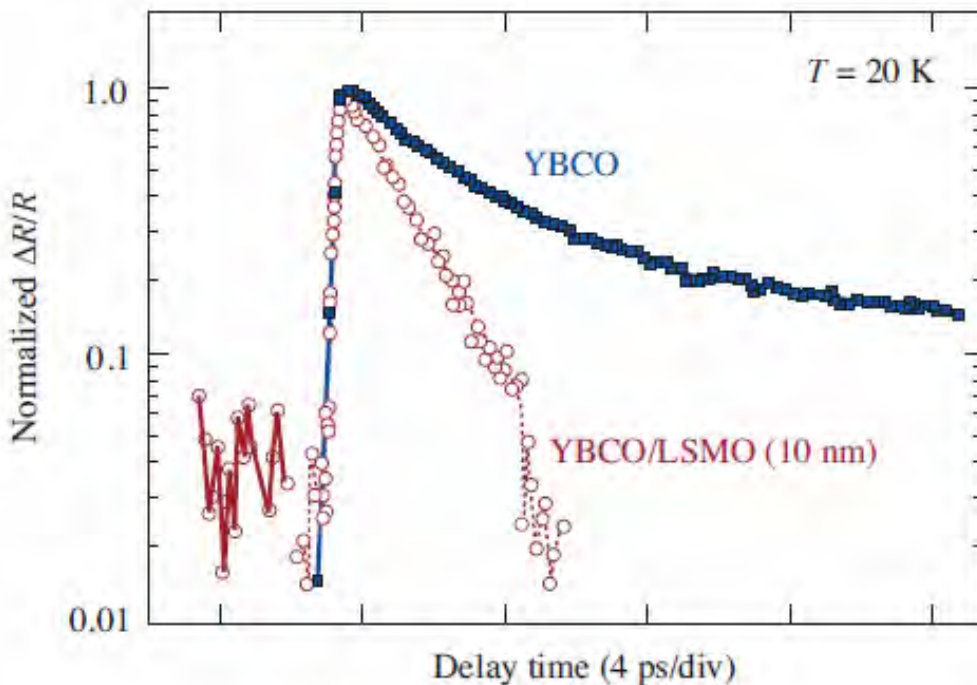


Figure 5.5 Time-resolved $\Delta R/R$ waveforms (semi-log scale) observed in a 100-nm YBCO thin film (black squares) and a LSMO (10 nm)/YBCO (100 nm) (red open circles) measured at $T = 20$ K.

Figure 5.6 shows our 3-T model fitting of LSMO/YBCO $\Delta R/R$ transient. We observe that there is a negative part of the $\Delta R/R$ transient which can not be properly modeled. However, the overall relaxation dynamics, as in the case of the NiCu/Au/YBCO (Fig. 5.3), is almost totally dominated by optical phonons (green line).

The negative relaxation component indicates that the phonon-escape mechanism must be different in all-oxide structures, as compared to the ones based on metallic F.

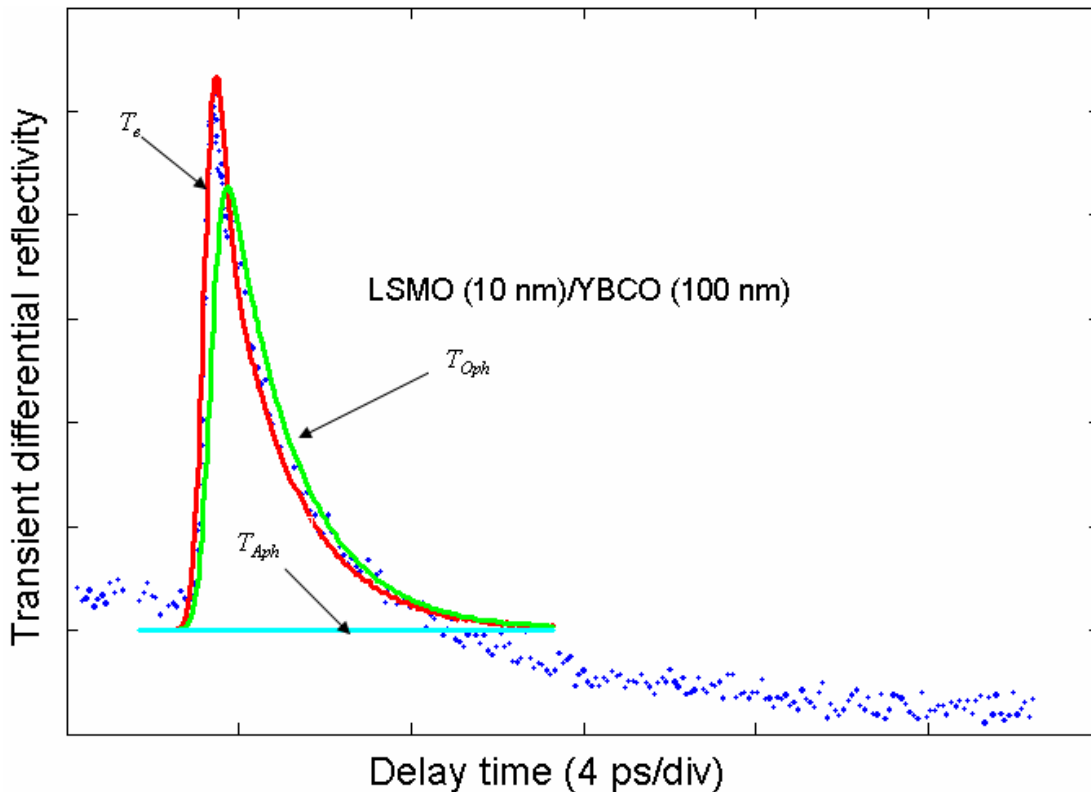


Figure 5.6 Numerical evaluation of the electron, optical phonon, acoustical phonon temperature transients for LSMO (10 nm)/YBCO (100 nm) bilayer using the 3-T model [see Eq. (2.26) to Eq. (2.28)].

Apparently, proximity effect makes the LSMO layer an effective sink layer for QPs coming from YBCO in parallel to the YBCO/substrate interface. It is important to note that we can expect an additional relaxation channel related to the spin interactions, due to the almost perfect half-metal nature of LSMO and the superconducting state of YBCO. Overall, the observed physical picture is very

interesting and, as in previous observations, an effective control the relaxation dynamics of the nonequilibrium superconducting state is clearly demonstrated. Moreover, our experiments involving epitaxial, oxide F/S heterostructures represent a new step toward better understanding of the proximity effect in oxide heterostructures and their potential applications [9,11]. A very likely presence of an under-doped YBCO layer at the interface with the LSMO overlayer adds an additional degree of freedom, as it was reported in Ref. [12].

5.3 Summary

We have presented the $\Delta R/R$ changes as a function of the time delay between the pump and the probe laser beams in F/S heterostructures formed by a HTS (YBCO) covered by Au/NiCu and manganite (LSMO) overlayers using all-optical femtosecond pump probe spectroscopy. The attention is mainly focused on the investigation of nonequilibrium excitation dynamics inside different bilayers in the temperature region well below T_c .

Our experiments are very preliminary, but they have demonstrated that, as compared to the pristine S films, the presence of a weakly F layer on top of the HTS induces a strong proximity effect between the F and S films, significantly modifying the QP dynamics of the heterostructures. From the experimental point of view, our HTS-based bilayers, the situation is quite similar to the NiCu/Nb bilayers, where the electron subsystem strongly dominated the nonequilibrium Cooper pair and QP dynamics, contrary to the pure Nb films, where the bolometric photoresponse was the most prevailing. The new element is that in YBCO optical phonons dominate the QP relaxation process, as it has been identified by simulations based on our 3-T model.

The above observations demonstrate that the F/S bilayers, both for LTS and HTS F/S heterostructures, could be considered as promising, novel “man-made” materials, in high-speed optical/radiation photodetectors. However, much more research is needed, which goes well beyond the scope of this thesis.

References:

-
- ¹ J. G. Bednorz and K. A. Müller, Possible high T_c superconductivity in the Ba-La-Cu-O system. *Z. Physik B*, 64, 189 (1986).
- ² A. Santoro, In High Temperature Superconductivity. *Springer-Verlag*, New York, (1990).
- ³ Z. Schlesinger, R. Collins, D. Kaiser, and F. Holtzberg. Superconducting energy gap and normal-state reflectivity of single crystal Y-Ba-Cu-O. *Phys. Rev. Lett.* 59, 1958 (1987).
- ⁴ V. V. Kabanov, J. Demsar, B. Podobnik, and D. Mihailovic. Quasiparticle relaxation dynamics in superconductors with different gap structures: Theory and experiments on YBCO. *Phys. Rev. B* 59, 1497 (1999).
- ⁵ G. A. Thomas, J. Orenstein, D. H. Rapkine, M. Capizzi, A. J. Millis, R. N. Bhatt, L. F. Schneemeyer, and J. V. Waszczak. Ba₂YCu₃O₇: Electrodynamics of crystals with high reflectivity. *Phys. Rev. Lett.* 61, 1313 (1988).
- ⁶ M. Lindgren, M. Currie, C. Williams, T. Y. Hsiang, P. M. Fauchet, R. Sobolewski, S. H. Moffat, R. A. Hughes, J. S. Preston, and F. A. Hegmann. Intrinsic picosecond response times of Y-Ba-Cu-O superconducting photodetectors. *Appl. Phys. Lett.*, 74, 853 (1999).
- ⁷ C. Williams, Y. Xu, R. Adam, M. Darula, O. Harnack, J. Scherbel, M. Siegel, F. A. Hegmann, and R. Sobolewski. *IEEE Trans. on Appl. Supercon.*, 11, 578 (2001).

-
- ⁸ J. H. Claassen, S. Adrian, and R. J. Soulen, Jr. Large non-linear kinetic inductance in superconductor/normal metal bilayer films. *IEEE Trans. Appl. Supercond.*, 9, 4189 (1999).
- ⁹ G. P. Pepe, D. Pan, V. Pagliarulo, L. Parlato, N. Marrocco, C. De Lisio, G. Peluso, A. Barone, U. Scotti di Uccio, A. Casaburi, F. Tafuri, M. Khafizov, T. Taneda, and Roman Sobolewski. Ultrafast Photoresponse of Superconductor/Ferromagnet Nano-Layered Hybrids. *IEEE Trans. Appl. Supercond.*, 19, 376 (2009)
- ¹⁰ D. Stornaiuolo, E. Gambale, T. Bauch, D. Born, K. Cedergren, D. Dalena, A. Barone, A. Tagliacozzo, F. Lombardi, and F. Tafuri. Underlying physical aspects of fluctuations in $\text{YBa}_2\text{Cu}_3\text{O}_{7-\delta}$. *Physica C*, 468, 310 (2008).
- ¹¹ Z. Sefrioui, D. Arias, V. Peña, J. E. Villegas, M. Varela, P. Prieto, C. León, J. L. Martinez, and J. Santamaria. Ferromagnetic/superconducting proximity effect in $\text{La}_{0.7}\text{Ca}_{0.3}\text{MnO}_3/\text{YBa}_2\text{Cu}_3\text{O}_{7-\delta}$ superlattices. *Phys. Rev. B*, 67, 214511 (2003).
- ¹² T. Gong, L. X. Zheng, W. Xiong, W. Kula, Y. Kostoulas, R. Sobolewski, and P. M. Fauchet. Femtosecond optical response of YBa-Cu-O thin films: The dependence on optical frequency, excitation intensity, and electric current. *Phys. Rev. B*, 47, 14, 495 (1993).

Chapter Six: Conclusions

6.1 Thesis summary and the main results

The proximity effect at F/S interfaces produces damped oscillatory behavior of the Cooper pair wave function within the ferromagnetic medium. The F/S nano-bilayers allow for coexistence of superconductivity and ferromagnetism. The presence of the weak ferromagnetic overlayer produces faster optical relaxation response, as compared to the sole superconducting films. In this thesis, investigations of the nonequilibrium carrier dynamics in the F/S heterostructures is the essential subject of our time-resolved, temperature-dependent transient optical reflectivity experiments and electrical photoimpedance measurements.

Our data modeling have shown that both 2-T model and RT model can effectively describe the nonequilibrium carrier dynamics of the photoresponse in the nanostructured F/S bilayers. Simultaneously, our own modeling extension, the 3-T model, by separating the phonon subsystem into optical-phonon and acoustical-phonon subsystems, allowed us to more actually describe the carrier relaxation dynamics in both the F/S and pure S systems resulting in better fits to the experimental photoresponse signals and somewhat deeper understanding of the physics.

We have reviewed our optical-characterization studies of novel proximized F/S nano-bilayers, using a time-resolved, all-optical, femtosecond pump–probe

spectroscopy technique. The weak ferromagnetic nature of the completely proximized F film makes it possible to observe the dynamics of the nonequilibrium superconductivity through the near-surface optical reflectivity change measurements. Our measurements were performed on both the metallic and oxide F/S nano-bilayers, ranging from pure Nb, NiCu/Nb, to NiCu/Au/YBaCuO and LaSrMnO/YBaCuO in a wide temperature range below and above T_c . The analysis of data with the 2-T and 3-T models in order to investigate the role of the proximity effect on the e - ph coupling constant in F/S heterostructures have been completed. Through the analysis of our experiment results, we have observed that a thin layer of weak ferromagnetic material strongly reduces the slow bolometric component of the superconductor film. The F/S samples exhibited the Cooper-pair and QP relaxation dynamics always significantly faster than that of the pure superconducting film (e.g., Nb or YBaCuO), which were strongly influenced by the “phonon bottleneck” effect.

We also performed the time-resolved photoimpedance measurements on current-biased microbridges to study the photoresponse mechanism in the pure superconducting material and the F/S hybrid. We characterized the resistive voltage response and kinetic inductive response for Nb and NiCu/Nb samples, respectively. In the Nb case, only under the high laser fluence condition, some slow signal (FWHM ≈ 10 ns) could be observed. However, in the NiCu/Nb structure, the much faster signal, (FWHM ≈ 700 ps limited by the front end electronic instrument) could be easily observed under much weaker laser fluence. Both experimental results have been fitted properly by the presented models.

Our photoimpedance measurements confirmed feasibility of using F/S microbridges as ultrafast radiation photodetectors, although so far we could not properly time-resolve the real photoimpedance signals due to the bandwidth limitations of our lab electronics.

We conclude that our research presented in the thesis demonstrates that F/S heterostructures are promising materials for new type of superconducting photodetectors and photon counters. We want to stress, however, that beside their applied interest, the F/S nano-layered hybrids are unique specimens for the fundamental studies of coexistence of superconductivity and magnetism as well as Cooper-pair and spin interactions in fully proximized oxide-based systems.

6.2 Directions for future work

We have studied the time-resolved dynamics of carriers in NiCu/Nb nano-bilayers with transient reflectivity experiment using all-optical pump-probe method and transient photoimpedance measurement across current-biased microbridges. However some results are limited by our front end electronic instruments. In the future work, using equipment with significantly better bandwidth and resolution capability would be one solution. We may also use the electro-optical sampling technique to obtain better time resolution of transient photoimpedance signals when the photoresponses are in the sub-picosecond range, as it has been demonstrated in other studies performed in our laboratory.

Further extensive and systematic experimental studies of photoresponse measurements on various new material components proximized nano-bilayers, such as PdNi/Nb, NiCu/Au/YBCO, Py ($\text{Ni}_x\text{Fe}_{1-x}$)/Nb, LASMO/YBCO etc., are needed to reach better understanding the proximity effect in F/S heterostructures. More theoretical insights into nonequilibrium carrier dynamics in oxide F/S bilayers is also needed. Especially the physics of how the proximity effect affects the early phase of the relaxation dynamics and later the QP recombination times in HTS materials based F/S nano-bilayers, such as a possibly of the additional relaxation channel related to the spin interactions in half-metal LSMO/YBCO bilayers, is very complex and needs to be further explored.

Besides the scientific interest, applications for superconducting materials are always the driving force for superconducting electronics, such as fast-detection and ultra sensitive devices. In this respect, however, new, reproducible fabrication of various F/S HTS-based nanowires needs to be developed first. Implementing meander-type nanostructures in proximized weak F/S nano-bilayers and estimating performance parameters of F/S radiation detectors, especially in the infrared range of optical radiation, would be a big step forward in terms of the fast photon counting operations.